Journal of Quantitative Spectroscopy & Radiative Transfer 267 (2021) 107561

Contents lists available at ScienceDirect

Journal of Quantitative Spectroscopy & Radiative Transfer

journal homepage: www.elsevier.com/locate/jqsrt

Light scattering by fractal roughness elements on ice crystal surfaces

Elina Riskilä [a], Hannakaisa Lindqvist [a], Karri Muinonen [b,c,*]

[a] Finnish Meteorological Institute, Erik Palménin aukio 1, Helsinki FI-00101, Finland
[b] University of Helsinki, Department of Physics, Gustaf Hällströmin katu 2, Helsinki FI-00560, Finland
[c] National Land Survey, Finnish Geospatial Research Institute FGI, Geodeetinrinne 2, Masala FI-02430, Finland

ARTICLE INFO

Article history:
Received 6 April 2020
Revised 18 September 2020
Accepted 3 February 2021
Available online 2 March 2021

MSC:
00-01
99-00

Keywords:
Light scattering
Rough surfaces
Ice crystals
DDA

ABSTRACT

Atmospheric ice crystals scatter sunlight, affecting Earth's climate through the radiation properties of cirrus clouds. Naturally occurring surface roughness and its effect on the scattering properties of ice crystals remain largely unknown. Scattering by ice crystals with rough surfaces is studied by placing a finite, thin surface-roughness element on an infinitely large, planar vacuum-ice boundary. The elements are generated using a statistical model based on fractional Brownian motion. The horizontal roughness scale is described by the Hurst exponent H and the vertical roughness scale with the root-mean-square roughness parameter R_q. The computations are performed with the surface mode of the Discrete Dipole Approximation software ADDA (version 1.34b). Several incident directions for wavelength of 0.5 µm from both above and below the planar surface are studied. A refractive index for ice $m = 1.313 + i5.889 \times 10^{-10}$ is used throughout the computations. Results are averaged over ten rough surface realizations for a specific H, R_q-pair.

Scattering by the rough elements is compared to that by the corresponding smooth elements. The rougher the element is, the more of the scattered intensity is transmitted through the surface. The rough elements have distinctively smoother angular distributions for the degree of linear polarization than their smooth counterparts. Also, it is found that while roughness itself affects polarization, the exact surface morphology does not seem to have a significant effect. The vertical roughness scale R_q has a larger effect on the light scattering results than the horizontal scale H. Enhanced angular scattering is detected in directions nearly parallel to the vacuum-ice boundary within the ice medium. The phenomenon is explained with a strong internal reflection mechanism.

The model for surface roughness, along with the light scattering methodology used here, could be incorporated into geometric optics ray-tracing computations for large ice crystals and other particles.

1. Introduction

Scattering of light by atmospheric ice crystals affects the radiation balance of the Earth-atmosphere system, and has an important role in many meteorological and remote sensing applications. The physical properties of ice crystals–size, shape, composition, and structure–determine their optical properties. In particular, ice crystal surface roughness affects many applications that rely on an accurate model of light scattering by ice crystals (e.g., [1,2]). Overall, the reflectance from ice clouds is a large uncertainty in climate models [3].

Atmospheric ice crystals are formed through cycles of different temperature and humidity conditions as they fall due to gravity, or rise to higher altitudes in updrafts. The size of an ice crystal varies from micrometer-scale up to several centimeters [4]. Ice crystal growth favors hexagonal shapes, which can grow into many different forms in varying temperature, pressure, and humidity conditions, or aggregate together to form even more complex shapes (for examples, see, e.g., [5]). Light scattering by different ice crystal shapes has been studied extensively (see, e.g., [6–8]). However, little is known about the surfaces of natural ice crystals and, hence, their effect on scattering. Atmospheric ice crystals can be studied in situ through airborne measurements, but the resolution is not sufficient for the micrometer-scale surface structures [9]. Instead, indirect methods such as the Small Ice Detector [10,11] or remote sensing measurements [12] are used but these methods rely on a numerical model of scattering by an ice crystal.

* Corresponding author.
E-mail addresses: elina.riskila@fmi.fi (E. Riskilä), karri.muinonen@helsinki.fi (K. Muinonen).

https://doi.org/10.1016/j.jqsrt.2021.107561

Scanning electron microscopes (SEM) can be used to obtain high-resolution images of ice crystals. Transporting intact crystals inside the microscope chamber is difficult, if not impossible, at least from high-altitude cirrus clouds. Thus, the crystals studied with SEM are usually grown inside the microscope chamber. Crystals are forced through several cycles of different temperature and humidity conditions to simulate growth and ablation in the atmosphere [13–16]. For example, Magee et al. [15] used a temperature range from −21 °C to −45 ° C and 105–125% relative humidity (with respect to ice). SEM images of crystal surfaces show strands, valleys, and lines formed on the crystal facets (see, e.g., [11,15]), and most crystals show anisotropic roughness [13–15]. Butterfield et al. [16] also retrieved micrometer-scale, three-dimensional representations of rough ice crystal surfaces obtained from SEM images, and studied how surface roughness depends on different environmental conditions. Both isotropic and anisotropic roughness was seen on crystal surfaces. Overall, surface roughness has been detected in all growth and ablation conditions the crystals were exposed to. However, no clear relationship between surface morphology and temperature or supersaturation has been found [15]. Also, different surface roughness has been observed between basal and prism facets. The size of the roughness features was 0.1–10 µm, most smaller than 1 µm [14,15]. Pfalzgraffet et al. [13] found strands between the prismatic facets of the crystal surfaces, separated by 5–10 µm. The scale of the observable roughness depends on the resolution of the microscope. Thus, nano-scale features have not been observed [15]. The coating procedure in SEM imaging may also affect the detection of roughness in the smallest scales.

While ice crystal surface roughness has been detected in a wide range of temperature and humidity conditions, it is not clear if atmospheric ice crystals will show similar surface morphology, as the conditions inside the SEM chamber are very different from those in the atmosphere [14]. A typical cirrus cloud is at altitudes with atmospheric pressure around 200 hPa, while the pressure inside the chamber is 50–200 Pa [14]. The crystals were usually grown in pure water vapor, while the atmosphere is a mixture of gases and aerosols. The range of humidity and temperature conditions used in the SEM experiments is also narrow compared to that observed in remote sensing studies [16]. The substrate the crystals are grown on can also have an effect on the crystal structure. However, Neshyba et al. [14] found that crystal edges not in contact with the substrate also showed signs of roughness, indicating that roughness was not caused by the substrate. Magee et al. [15] did not find a correlation between the roughness features and the substrate the crystals were grown on. They also studied crystals grown outside the chamber in air–water vapor mixture and pressure of 1000 hPa. Transported crystals showed similar roughness features than chamber-grown crystals, indicating that surface roughness was not affected by the growth conditions inside the SEM chamber alone. However, there were some differences, most notably that the transported crystals showed more smooth features on the crystal surfaces than the chamber-grown crystals. Current developments and novel instrumentation introduced by Magee et al. [17] will provide interesting possibilities for further research on surface roughness of natural ice crystals.

Because of the aforedescribed variety in the physical properties, scattering by atmospheric ice crystals cannot be solved analytically but an approximate method is needed. The method chosen depends primarily on the relation of the radius a of the scatterer to the wavelength λ of the incident light, which is described by the size parameter $x = 2\pi a/\lambda$. For many atmospheric applications regarding scattering by ice crystals, $x \gg 1$, and, thus, geometric optics is often used for computing scattering by ice crystals (e.g., [18] and references therein). In geometric optics, scattering computations trace the paths of individual rays that are reflected and transmitted as they interact with the surface of the scatterer. Essentially, it is required that all geometric features of the particle are large compared to the wavelength of incident light. However, given surface roughness of the scale observed in the SEM images, geometric optics cannot be used for all size parameters relevant for ice crystals in the atmosphere. The effect of ice crystal surface roughness has traditionally been described by the so-called tilted-facet algorithm, where the geometric optics model is altered in a way that every time a light ray encounters a boundary, the reflections and refractions are computed from a facet tilted randomly from the normal of the surface [6,7,19,20]. The tilt angle is chosen based on an assumed probability distribution of surface heights, usually following either a normal or Weibull distribution. Many features of the scattered light can be explained by using the random-tilt algorithm: surface roughness smoothens the angular distributions of scattering quantities [8,20]. Halos from hexagonal ice crystal scattering intensity maxima at 22° and 46° diminish, and disappear completely with substantial roughness [21]. However, the random-tilt model is not a physical model of roughness. It only simulates the effect of some randomization in the planar facets of ice crystals, and does not account for the small-scale structure. In fact, inconsistencies between observations and random-tilt simulations have been reported [16,22]. In addition, similar smoothening of the scattering quantities can also be caused by distortion of particle shape [8], or by physical optics effects in the case of smaller ice crystals with size parameters of $x \sim 25$ [23]. It may be difficult to discriminate between these effects.

There have been recent developments on the Modeling of ice crystal surface roughness by using a Gaussian surface, which represents the surface as a superposition of Fourier modes with random phase [24,25]. While the Gaussian surface is a more realistic representation for a rough surface than the random-tilt model, the problem remains that scattering cannot be computed for all the relevant size parameters. Liu et al. [24] used the geometric optics model for larger size parameters, but it cannot take into account the finer structures of surface morphology. Collier et al. [25] computed light scattering for a roughened ice crystal in the discrete-dipole approximation (DDA) using the Amsterdam Discrete Dipole Approximation (ADDA) code for size parameters up to $x = 100$, observing smoothening of the scattered intensity for rougher crystals, with an increasing effect for larger size parameters. Forward direction of scattering was found to be less sensitive to roughness than the backward direction. However, at the wavelengths of visible light, $x = 100$ corresponds to an ice crystal with a radial distance of ~ 10 µm, while ice crystals can reach sizes of 100–1000 µm [4]. Larger size parameters are challenging to reach with ADDA due to computational limitations. Thus, it is not possible to account for all the size parameters representing ice crystals. ADDA can, however, be used to compute scattering by small-scale surface features, and is therefore a good candidate for light scattering by rough surfaces. In fact, Parviainen and Lumme [26] used ADDA to compute light scattering by circular films with roughened surfaces.

Light scattering by rough surfaces has traditionally been studied using approximate methods, with exact methods becoming more popular as computational capabilities increase (see [27] for a thorough review of scattering by rough surfaces). Compared to a smooth surface, scattering by rough surfaces is generally more diffuse. The angular distributions of scattered quantities smoothen, and the scattered intensity decreases with increasing roughness (see, e.g., [19,28,29]). Also, phenomena not seen with smooth surfaces such as backscattering enhancement (Maradudin [27]; coherent backscattering, see also Lindell et al. [30], Muinonen et al. [31]) and so-called optical counterparts of the Yoneda X-ray peaks [32–34] can be found.

Light scattering by rough surfaces is an extensive field of research, with many applications in physics and engineering. Exam-

ples include materials science [35] and remote sensing of land surfaces [36] or snow-covered ground [37]. In astronomy, the surfaces of atmosphereless planetary bodies can also be described using random rough surfaces (see, e.g., [38]). There is a multitude of numerical models for the treatment of light scattering by rough surfaces. For example, methods for computing scattering by atmospheric dust particles with rough surfaces can be found in, e.g., [39,40], and [28].

Our work focuses on studying the effect of a surface-roughness element on light scattering by ice crystal surfaces. The roughness model based on fractional Brownian motion – a widely used method for surface roughness simulations in other fields – is here used for the first time for ice crystal surface roughness, providing a realistic representation of a surface-roughness element. The method has been utilized, for example, in material technology, with the purpose of generating rough pavement surfaces based on measured roughness parameters [35]. The surface-roughness element, now composed of ice, is located on a planar ice surface. Scattering quantities are computed using the surface mode of ADDA, hereafter ADDA-S. The computations are done assuming single scattering of visible light by macroscopic ice particles, with the medium outside of the scatterer comparable to a vacuum. Even though ADDA has been used for computing scattering by ice crystals with rough surfaces [25], ADDA-S has not been previously applied to ice crystals. ADDA-S provides a scattering model suitable for the wavelength-scale features in rough ice crystal surfaces that geometric optics cannot account for. Scattering computations performed for different rough surfaces give insight into the sensitivity of the scattering quantities to the roughness parameters, which in turn can provide information on what kind of parameters should be obtained from real ice crystal surfaces in order to estimate their optical properties.

The paper consists of five sections. The theoretical and methodological backgrounds are introduced in Section 2, including numerical methods for generating the surface-roughness elements and the model used to compute scattering. Results from the scattering computations are presented in Section 3 and discussed in Section 4. Conclusions are presented in Section 5.

2. Theoretical and numerical methods

2.1. Light scattering theory

The scattering Mueller matrix relates the Stokes parameters I, Q, U and V of the incident (subscript i) and scattered (s) fields (see, e.g., [41]):

$$\begin{bmatrix} I_s \\ Q_s \\ U_s \\ V_s \end{bmatrix} = \frac{1}{k^2 r^2} \begin{bmatrix} S_{11} & S_{12} & S_{13} & S_{14} \\ S_{21} & S_{22} & S_{23} & S_{24} \\ S_{31} & S_{32} & S_{33} & S_{34} \\ S_{41} & S_{42} & S_{43} & S_{44} \end{bmatrix} \begin{bmatrix} I_i \\ Q_i \\ U_i \\ V_i \end{bmatrix}, \tag{1}$$

where r is the distance between the scatterer and the observer and $k = 2\pi/\lambda$ is the wave number (λ is the wavelength). The elements S_{ij} are functions of the scattering angle θ and the azimuthal scattering angle ϕ. If the incident field is known, properties of the scattered field can be derived using the scattering matrix.

For unpolarized incident light, the Stokes parameters I_s and Q_s are

$$I_s = \frac{I_i}{k^2 r^2} S_{11}, \tag{2}$$

$$Q_s = \frac{I_i}{k^2 r^2} S_{21}. \tag{3}$$

In what follows, we will focus on the angular dependences of the scattering matrix elements S_{11} and S_{21}.

2.2. Rough surface generation

Self-similar, scale-independent features characteristic to fractal geometry can be found in natural surfaces such as rock surfaces, terrain, or planetary objects [38,42,43]. Realistic representations of rough surfaces can be generated using methods based on fractional Brownian motion or fBm [44]. As there is little evidence of natural ice crystal surfaces, fBm surface is here considered as a good candidate for ice crystal surface roughness, because the model physically resembles some of the processes that are responsible for surface roughness, for example diffusional sedimentation (depositional growth).

The fractal dimension D is related to the scale of the self-similar features: under magnification, shapes scaled down by a factor $\propto 1/D$ can be seen in fractal geometries.

In two dimensions, the height variations of a function $z(x, y)$ in the xy-plane along a straight line can be considered fractional Brownian motion if at a distance $\Delta r^2 = \Delta x^2 + \Delta y^2$ the surface height variation Δz is given by a power law:

$$\Delta z \propto \Delta r^H, \tag{4}$$

where the exponent H is related to the fractal dimension by $H = 3 - D$. H is known as the Hurst exponent [38] and can obtain values within [0,1]. Small values of H correspond to rougher surfaces, and values closer to 1 indicate smoother surfaces. $H = 0.5$ corresponds to Brownian motion.

Surfaces based on fBm can be generated by Fourier filtering using the spectral density S of $z(x, y)$ [44]. In two dimensions, S will depend on two frequency variables u and v corresponding to x and y. As all directions $r^2 = x^2 + y^2$ in the two-dimensional case are isotropic, i.e., equivalent with respect to statistical properties, S will depend on u and v:

$$S \propto \sqrt{u^2 + v^2}. \tag{5}$$

In the frequency domain, S is again a power law depending on the Hurst exponent:

$$S \propto \frac{1}{(\sqrt{u^2 + v^2})^{2(H+1)}}. \tag{6}$$

However, for real, infinite fBm surfaces, the standard deviation of the surface heights approaches infinity. In what follows, we make use of the self-affine Gaussian random rough surfaces on a finite base area as a proxy of infinite fBm surfaces. For more detailed information about random rough surfaces, we refer the reader to the works by, e.g., Simonsen et al. [45] and Yordanov and Atanasov [46].

Rough surfaces are here generated using a Matlab program called Artificial Surface [35] based on the Gaussian random rough surface concept for a finite surface element presented by Persson et al. [47]. Artificial Surface utilizes the Fourier filtering method for generating isotropic fBm surfaces. Grid sizes and length scales in the x- and y-directions are given as input parameters.

The program generates a rough surface based on the roughness parameters given as an input. The horizontal roughness scale is described by the Hurst exponent H. However, if a fractal roughness profile is stretched in the z-direction, the roughness of the surface is increased while the fractal dimension remains unchanged [48]. Therefore, a second parameter is needed to describe the surface heights. In the Artificial Surface, the ensemble-averaged root-mean-square of surface heights is used [49]:

$$R_q = \sqrt{< \frac{1}{A} \int \int_A [z(x, y)]^2 dx dy >}, \tag{7}$$

where A is the base area of the surface in the xy-plane. As R_q is directly related to the surface height profile, increasing R_q will result in a rougher surface. The Artificial Surface program further allows the utilization of the so-called roll-over wave number q_0 (see

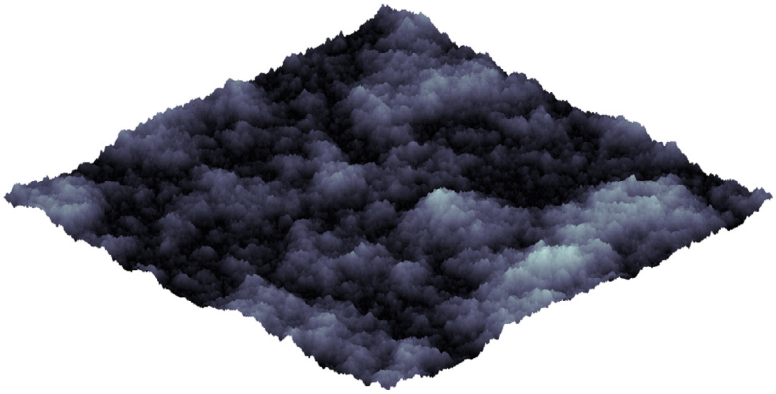

Fig. 1. An example of a 5 µm × 5 µm rough surface generated with roughness parameters $H = 0.5$ and $R_q = 0.1\,\mu m$.

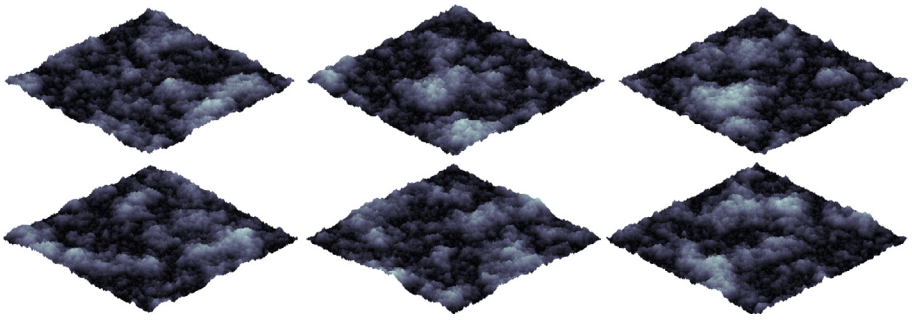

Fig. 2. Different surface realizations with roughness parameters $H = 0.5$ and $R_q = 0.1\,\mu m$.

[47,49]). However, it is here fixed to the value of $q_0 = 0$ throughout the work. The wave number domain is constrained by the size of the finite rough surface on the xy-plane, say $L \times L$, and the discretization of the realizations for scattering computations, that is, the dipole size d that equals the distance between two adjacent dipoles (see Section 2.3 below):

$$\frac{2\pi}{L} \leq q \leq \frac{\pi}{d}, \tag{8}$$

where π/d is the Nyqvist frequency.

The Artificial Surface program generates the rough surface by first generating two wave vectors corresponding to x and y directions based on the grid spacing given as input. A grid is generated and transformed to polar coordinates (φ, ρ), replacing φ with a random phase. The spectral density S is generated by using the power law in Eq. (6). Spectral density is then scaled in order to obtain the desired root-mean-square roughness R_q:

$$S_{\text{scaled}} = \frac{R_q}{R_{q,0}} S, \tag{9}$$

where $R_{q,0}$ is the root-mean-square roughness of the surface corresponding to the original S. Finally, the surface topography is brought to the xy-domain by applying inverse Fast Fourier Transformation to the spectral density S_{scaled}. An example of a surface generated with roughness parameters $H = 0.5$ and $R_q = 0.1\,\mu m$ is shown in Fig. 1. Due to the randomness of the phase, two surfaces with the same input parameters are not equal (see Fig. 2), but follow the same shape statistics.

2.3. The discrete dipole approximation

Light scattering calculations were performed using the DDA method. The program used is a C implementation of the DDA known as ADDA [50], more specifically a publicly available beta version (1.34b) ADDA-S that can calculate scattering by a particle near a plane surface [51]. The calculations were performed with the Voima supercomputer at the Finnish Meteorological Institute.

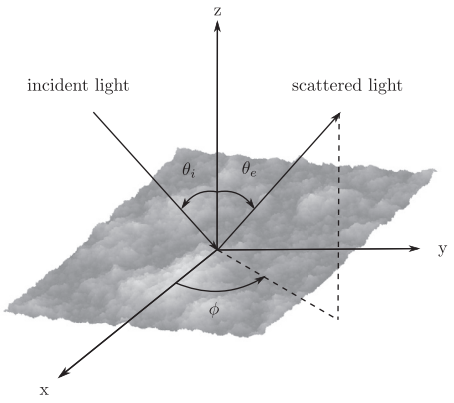

Fig. 3. The coordinate system used in ADDA-S. The direction of the incident light θ_i can be defined and given as an input. θ_e is the angle of emergence and ϕ is the azimuth angle. Figure is based on [54].

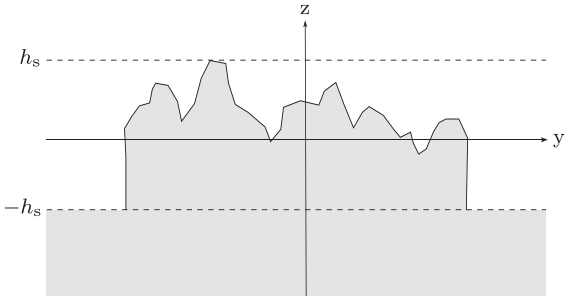

Fig. 4. Placement of the surface-roughness element on the planar ice surface. The surface is aligned with the xy-plane of the ADDA-S coordinate system, at $z = -h_s$.

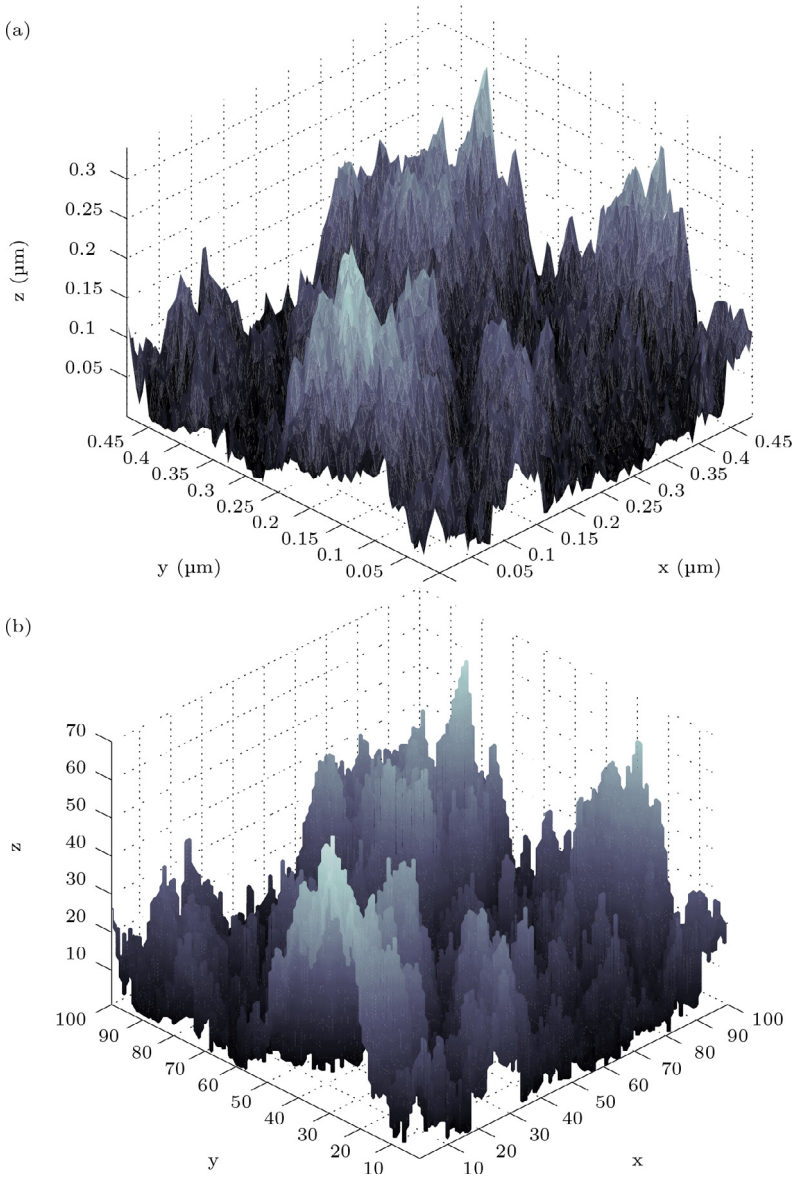

Fig. 5. (a) A segment with edge length 0.49 µm of a surface-roughness element such as those defined in Section 2.2. The surface was generated with roughness parameters $H = 0.5$ and $R_q = 0.1\,\mu m$. (b) The same surface, discretized for ADDA-S input (only the surface points are shown in the figure). The base is 100×100 dipoles, with maximum height of 70 dipoles.

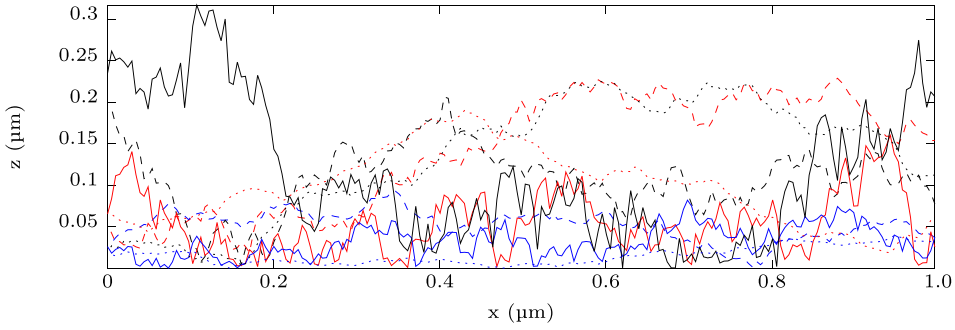

Fig. 6. Two-dimensional height profiles of surface-roughness elements generated with all nine combinations of roughness parameters, indicated by blue ($R_q = 0.05\,\mu m$), red ($R_q = 0.1\,\mu m$), and black colors ($R_q = 0.15\,\mu m$) and by solid ($H = 0.3$), dashed ($H = 0.5$), and dotted lines ($H = 0.7$). Note that the horizontal and vertical axes are in scale and that the actual edge length of the surface element is five times larger at 5 µm. See Fig. 4.

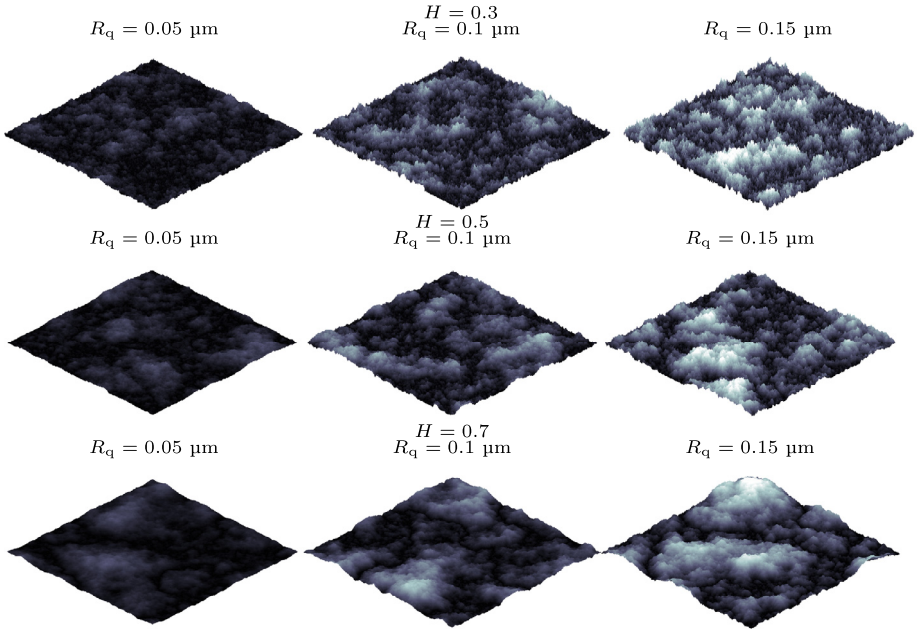

Fig. 7. Examples of rough surfaces generated with all nine combinations of roughness parameters $H = 0.3, 0.5, 0.7$ and $R_q = 0.05, 0.1, 0.15\,\mu m$. The colouring scale used is the same for all the images.

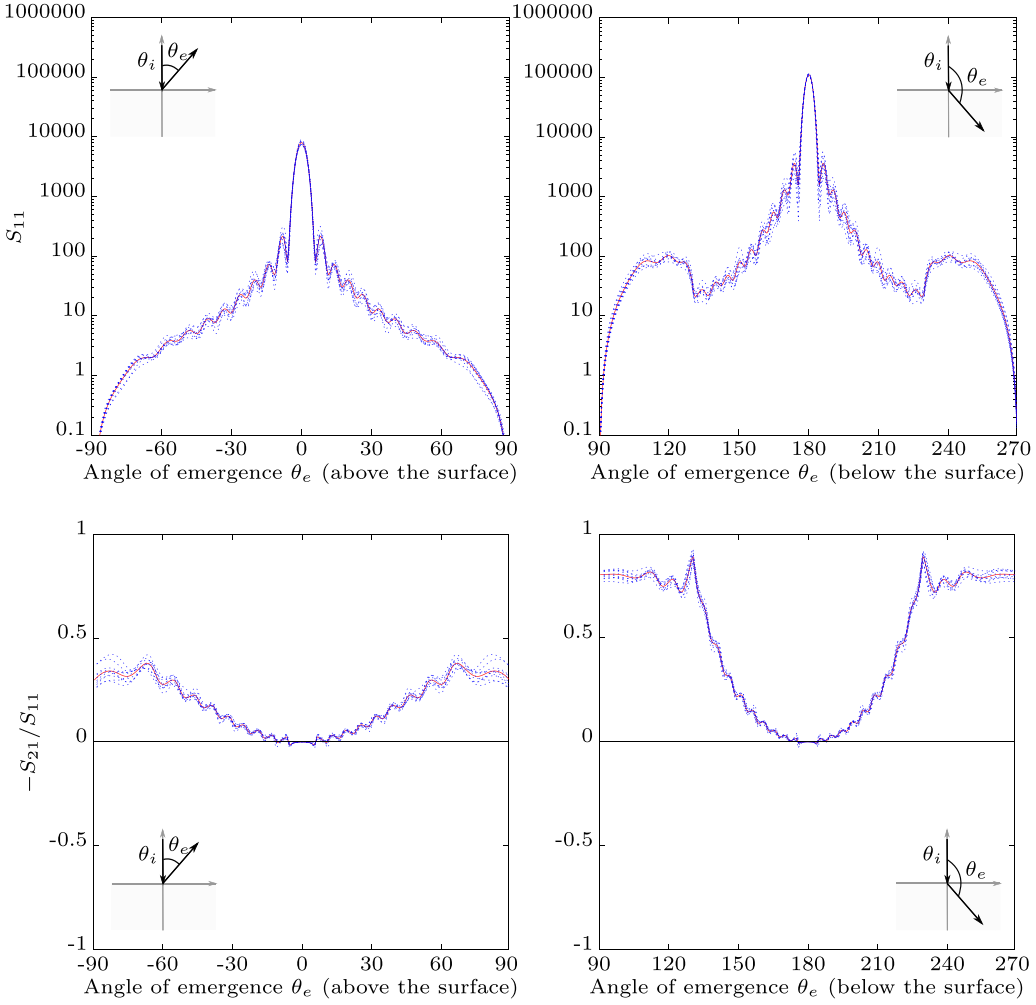

Fig. 8. Scattered intensity S_{11} and the degree of linear polarization $-S_{21}/S_{11}$ for unpolarized incident light, for ten surface-roughness elements with roughness parameters $H = 0.5$ and $R_q = 0.1\,\mu m$ above the surface (left) and below the surface (right). Different element realizations are represented with blue dotted lines, and averages over the ten realizations with a red solid line. Incident light is propagating in the *xz*-plane from above the surface along the *z*-axis. Results have been averaged over the azimuth angle ϕ. Values of $S_{11} < 0.1$ have been omitted for illustrative purposes.

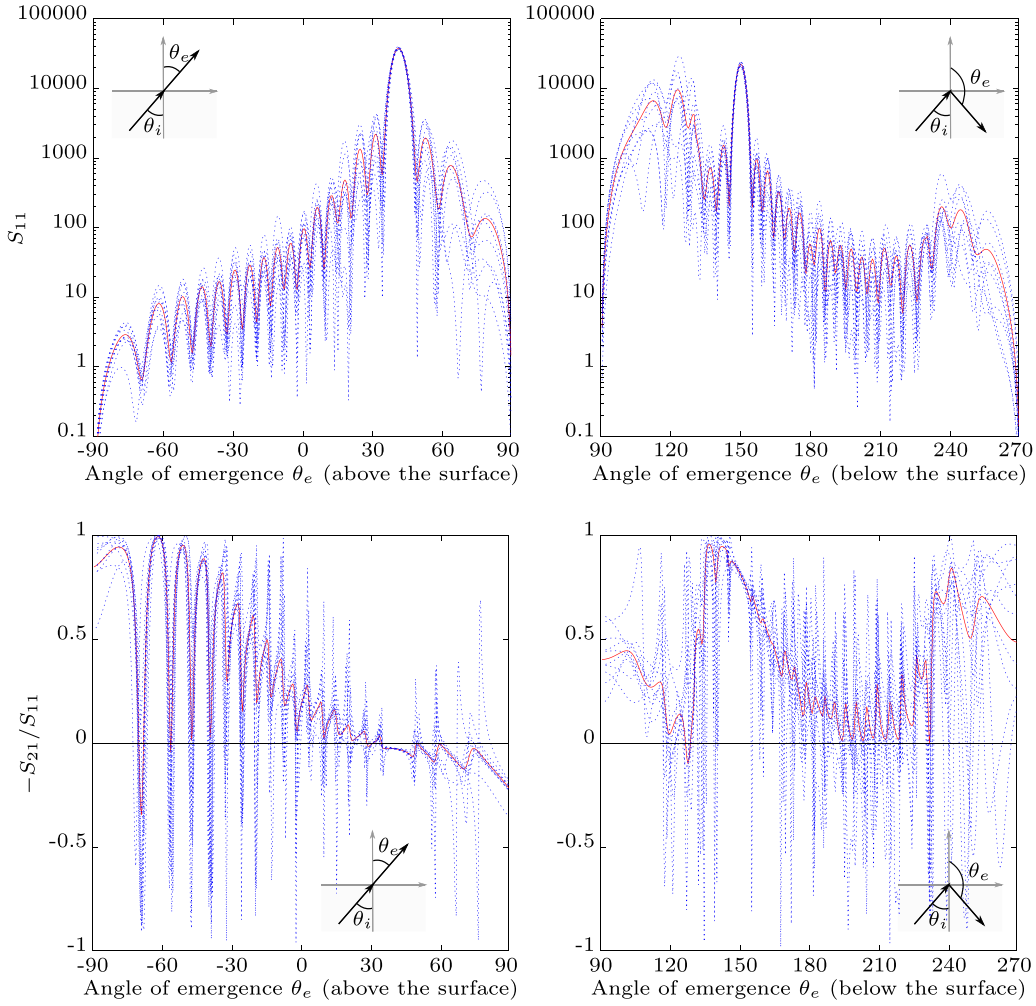

Fig. 9. As in Fig. 8, but with incident light propagating from below the surface at a 30° angle with respect to the z-axis, with $\phi = 0°$ (no averaging over the azimuth angle).

The DDA is suitable for particles either of the size of or smaller than the wavelength of the incident light, although the size parameter is limited only by the computer resources available [50]. In the DDA, the scatterer is represented by a set of interacting dipoles. There is a number of different DDA formulations. The equations presented here follow the point-dipole formalism; for an overview of the different DDA formulations, see [52].

The scatterer is assumed dielectric, but not magnetic: $\mu = \mu_0$ [52]. The incident electric field $\mathbf{E}_{\text{inc}}$ is assumed to be a plane wave with a harmonic time dependence:

$$\mathbf{E}_{\text{inc}}(\mathbf{r}) = \mathbf{E}_0 \exp(\mathrm{i}\mathbf{k}\cdot\mathbf{r} - \mathrm{i}\omega t). \tag{10}$$

For a dipole i located in $\mathbf{r}_i$ with polarizability $\boldsymbol{\alpha}_i$ [52], the total dipole polarization $\mathbf{P}_i$ is

$$\mathbf{P}_i(\mathbf{r}_i) = \boldsymbol{\alpha}_i \mathbf{E}_{\text{tot},i}, \tag{11}$$

where the total electric field $\mathbf{E}_{\text{tot},i}$ at dipole i's position is a sum of the incident plane wave (Eq. (10)) and a contributing factor from all dipole interactions [50]

$$\mathbf{E}_{\text{tot},i}(\mathbf{r}_i) = \mathbf{E}_{\text{inc},i} + \sum_{i\neq j} \mathbf{G}_{ij}\mathbf{P}_j, \tag{12}$$

where $\mathbf{G}_{ij}$ is a free-space Green's tensor. Substituting Eq. (11) into Eq. (12) gives a set of linear equations for N dipoles:

$$\mathbf{E}_{\text{inc},i}(\mathbf{r}_i) = \boldsymbol{\alpha}_i^{-1}\mathbf{P}_i - \sum_{i\neq j} \mathbf{G}_{ij}\mathbf{P}_j. \tag{13}$$

These are the main equations for the DDA [50]. They describe how the dipoles interact with each other and the incident electric field $\mathbf{E}_{\text{inc}}$. Total dipole polarizations $\mathbf{P}_i$ can be obtained by solving Eq. (13), and once the polarizations are known, the scattering matrix (Eq. (1)) can be derived for a set of predefined angles θ and ϕ.

The DDA can be applied to particles of arbitrary shape and composition. The only limitation for irregularly shaped particles is that the dipole size d should be small compared to the wavelength and any characteristic dimension of the particle itself. The size of one dipole should be [50]

$$d \leq \frac{\lambda}{10|m|}, \tag{14}$$

where m is the refractive index of the scatterer. To achieve desirable accuracy, $|m-1| < 2$ [50]. For particles with dimensions smaller than the wavelength, d should also describe the particle shape accurately [50]. This had to be taken into account when the roughness parameters R_q and H were chosen, so the dipole size could be kept constant throughout the simulations.

The DDA is a numerically exact technique: it is a direct consequence of the Maxwell equations [41], and its accuracy is limited only by the discretization resolution and, therefore, the computational resources available [51]. Accuracy studies of the DDA can be found in, e.g., [53], where the accuracy for intensity was found to be 2–6%, and 1–3% for the degree of linear polarization. Decreasing dipole size and thus increasing the total number of dipoles N improves the accuracy of the DDA. However, computational limita-

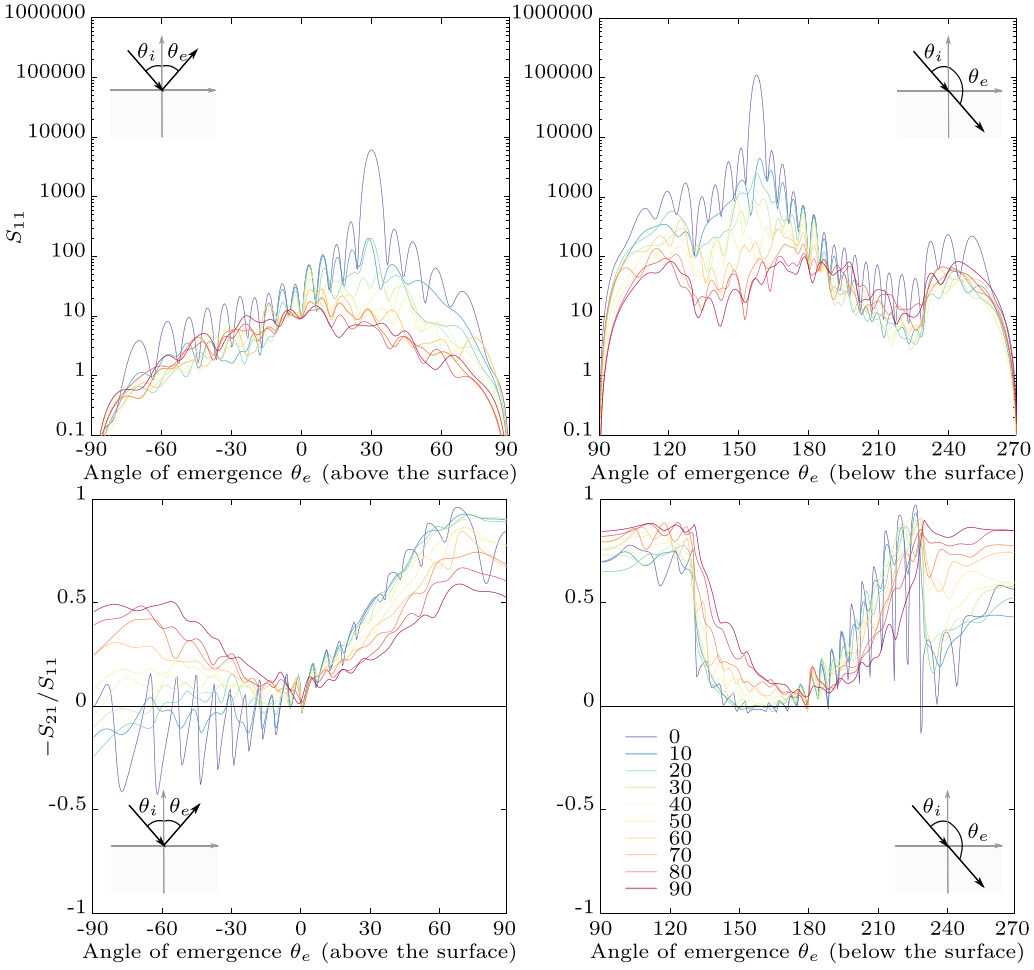

Fig. 10. Scattered intensity S_{11} and degree of linear polarization $-S_{21}/S_{11}$ for unpolarized incident light above the surface (left) and below the surface (right), averaged over ten realizations of surface-roughness elements with roughness parameters $H = 0.5$ and $R_q = 0.1\,\mu$m for different values of the azimuth angle ϕ ($0^\circ - 90^\circ$ in 10° increments). Incident light is propagating in the xz-plane from above the surface at a 30° angle with respect to the z-axis. Values of $S_{11} < 0.1$ have been omitted for illustrative purposes.

tions cause restrictions to N. Another thorough review on the accuracy studies of the DDA can be found in Yurkin and Hoekstra [52].

2.4. DDA near a planar surface

In addition to the free-space mode described in Section 2.3, ADDA can be used to calculate light scattering by a particle located above an infinite planar boundary between two homogeneous media [54]. The scatterer is placed at a distance h_s from the surface. All scattering calculations in this paper were done with ADDA-S, by placing a finite, thin surface-roughness element (see Section 2.5 for how the element is created) on top of a planar ice crystal surface. The crystal is assumed to be much larger than the surface element. Only pure ice without inclusions or any material attached to the surface was considered. In the surface mode, only the scatterer is discretized [51]. The incident electric field is different from that in the free-space mode due to the effect of the surface. Consider the plane surface without the scatterer. When the incident light comes from above the surface, $\mathbf{E}_{\text{inc}}$ now consists of the incoming field $\mathbf{E}_{\text{in}}$ in Eq. (10), and a part reflected from the surface [51]:

$$\mathbf{E}_{\text{inc}} = \mathbf{E}_{\text{in}} + \mathbf{E}_{\text{refl}}. \tag{15}$$

Similarly, when the incident light comes from below the surface, $\mathbf{E}_{\text{inc}}$ now only consists of the transmitted part:

$$\mathbf{E}_{\text{inc}} = \mathbf{E}_{\text{trans}}. \tag{16}$$

The incident electric fields in Eqs. (15) and (16) are now those that interact with the scatterer.

The effect of the surface on dipole interactions is taken into account by replacing the free-space Green's tensor $\mathbf{G}$ with $\mathbf{G}+\mathbf{R}$, where $\mathbf{R}$ is the part induced by the surface [51]. The set of linear equations (Eq. (13)) now becomes (see supporting information in Yurkin and Huntemann [51] for details):

$$\mathbf{E}_{\text{inc},i}(\mathbf{r}_i) = \boldsymbol{\alpha}_i^{-1}\mathbf{P}_i - \sum_{i\neq j}(\mathbf{G}_{ij} + \mathbf{R}_{ij})\mathbf{P}_j. \tag{17}$$

Scattering quantities can now be calculated after solving the dipole polarizations $\mathbf{P}_i$ from Eq. (17). Yurkin and Huntemann [51] presented definitions for the amplitude scattering matrix and the scattering matrix for a scatterer near a surface, where the electric fields in the amplitude scattering matrix are replaced with those in Eqs. (15) and (16). Similarly, the Stokes parameters for incident light are defined as I_{in}, Q_{in}, U_{in} and V_{in}, consisting of an incoming and reflected part for incident light coming from above the surface, and a transmitted part for incident light coming from below the surface.

The scattering geometry of ADDA-S is fixed (Fig. 3): the xy-plane is aligned with the surface and the origin is in the center of the scatterer [54]. Scattering by a surface-roughness element on a large ice crystal could be calculated by placing the element exactly on the surface, making sure that there is no empty space between the scatterer and the surface. In ADDA-S, the scatterer cannot be

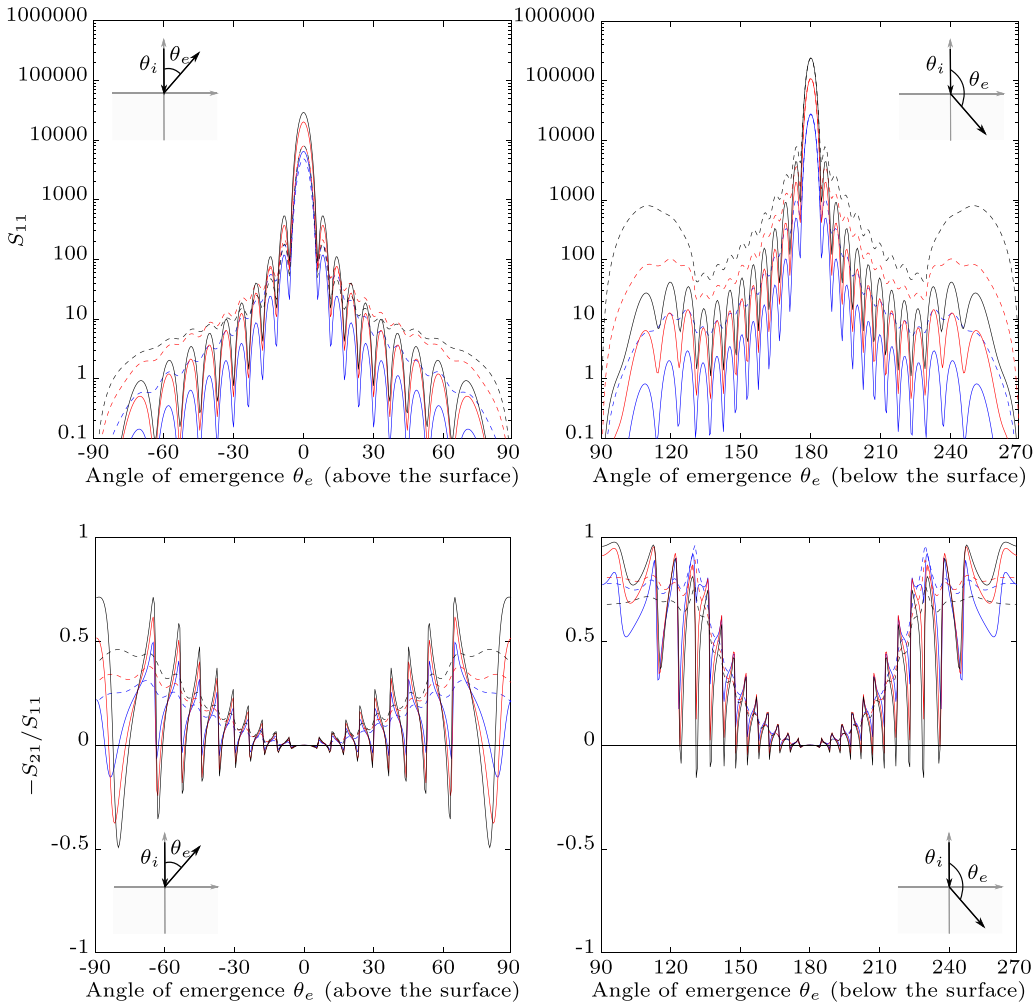

Fig. 11. Scattered intensity S_{11} and the degree of linear polarization $-S_{21}/S_{11}$ for unpolarized incident light above the surface (left) and below the surface (right) for smooth elements with a total number of dipoles corresponding to $R_q = 0.05\,\mu m$ (a blue solid line), 0.1 μm (a red solid line) and $0.15\,\mu m$ (a black solid line), and rough elements with $H = 0.5$ and $R_q = 0.05\,\mu m$ (a blue dashed line), 0.1 μm (a red dashed line), and $0.15\,\mu m$ (a black dashed line). Incident light is propagating in the xz-plane from above the surface along the z-axis. Results have been averaged over the azimuth angle ϕ. Values of $S_{11} < 0.1$ have been omitted for illustrative purposes.

partially submerged in the planar surface [51]. The height from the surface h_s was calculated using the maximum height of the surface element z_{max}:

$$h_s = \frac{1}{2} \cdot z_{max}. \tag{18}$$

The surface is aligned with the xy-plane at $z = -h_s$ (Fig. 4).

It should be noted that the surface mode is still under development and only appears in the beta version 1.34b of the ADDA code. Hence, there were some restrictions to the calculations: most importantly, the physical size of the scatterer could not be larger than 5 μm regardless of the total number of dipoles. Even with smaller dipole sizes the calculations were not possible. Orientation averaging was not available [54], meaning that different incident light propagation directions needed to be calculated separately. Also, a systematic accuracy study such as that described in Section 2.3 has not been done on ADDA-S [51].

2.5. Discretizing the scatterer

In ADDA, the scatterer is discretized by dividing it into cubic elements which represent the dipoles. The computational grid of ADDA will consist of cubes, where the edge of a cube d is the dipole width [50]. By constructing an appropriate dipole set by dividing the scatterer into small cubic subvolumes, an arbitrary shape can be given to ADDA as an input [54]. A refractive index is then assigned to each dipole [50].

The surfaces defined in Section 2.2 were discretized with a Matlab program written for this purpose. The program generates a file in the ADDA input format specified in Yurkin and Hoekstra [54] by making a grid with a predefined number of cubic elements. Here, a grid size of $1024 \times 1024 \times z_{max}$ was chosen, where a maximum height z_{max} (in dipoles) is given as input to the discretization program. With a given maximum height, only one h_s needed to be calculated for each set of surfaces with a given (H, R_q)-combination, thus simplifying the calculations.

A dipole is generated for all grid points with $z \leq z_{surf}$, where z_{surf} is the rough surface generated by Artificial Surface. ADDA will then assign a dipole to the scatterer as long as the center of a dipole is inside the particle shape [54]. This was taken into account while specifying h_s, making sure there were no void dipoles between the surface element and the planar surface. The dipole size is defined directly from the grid size used in the Artificial Surface program (see Section 2.2 for details), and kept constant throughout the simulations. The values for the roughness parameters, z_{max}, and h_s used here are presented in Table 1.

A close-up of a surface element (edge length of the element 0.49 μm corresponding to 100 dipoles) with $H = 0.5$ and $R_q = 0.1\,\mu m$ is shown in Fig. 5(a). The same surface in discretized form

Table 1
Roughness parameters H and R_q, maximum grid height z_{max} and height from the planar surface h_s used in computations. The total number of dipoles in the computational volume of the DDA equals $z_{max} \times 1024 \times 1024$, where the unit for z_{max} is the number of dipoles.

	R_q (μm)	z_{max} (dipoles)	h_s (μm)
$H = 0.3$	0.05	40	0.0977
	0.1	84	0.205
	0.15	120	0.295
$H = 0.5$	0.05	34	0.0830
	0.1	70	0.171
	0.15	110	0.269
$H = 0.7$	0.05	32	0.0781
	0.15	100	0.244

(base 100×100 dipoles) can be seen in Fig. 5(b). Note that the figures show only surface points, not the fully constructed volume of the element. As can be seen in the figures, some of the finer structures in surface morphology will be lost when the surface is discretized.

3. Results

Results from the scattering calculations carried out with ADDA-S are presented in this section. The surface-roughness elements generated with different roughness parameters are discussed in Section 3.1. First, some testing of ADDA-S is performed: the effect of averaging over different surface realizations, along with scattering results for different azimuth angles ϕ, are presented in Section 3.2. In Section 3.3, scattering by smooth and rough elements is compared. Finally, scattering results for elements generated with different roughness parameters are shown in Section 3.4.

Results were averaged over the azimuthal angle ϕ when possible, i.e., when the incident light was propagating in the direction normal to the surface. Resolution used for the angle of emergence θ_e was 0.5°, and 1° for the azimuth angle ϕ. Wavelength of the incident light was chosen to be 0.5 μm, corresponding to visible light. The refractive index used for both the surface-roughness element and the infinite planar surface located below it was $m = 1.313 + i5.889 \times 10^{-10}$ [55]. These, along with the dipole size, were kept constant throughout the computations.

3.1. Surface-roughness elements

Surface-roughness elements have been generated with the Artificial Surface Matlab program described in Section 2.2 with several different values for the roughness parameters R_q and H. The surface elements used in the computations have been generated by applying the volume discretization described in Section 2.5. For the final computations, a square base with an edge length of 5 μm was chosen. Grid size was selected to be 1024 for both x and y-directions, which corresponds to a dipole size of $d = 4.9$ nm.

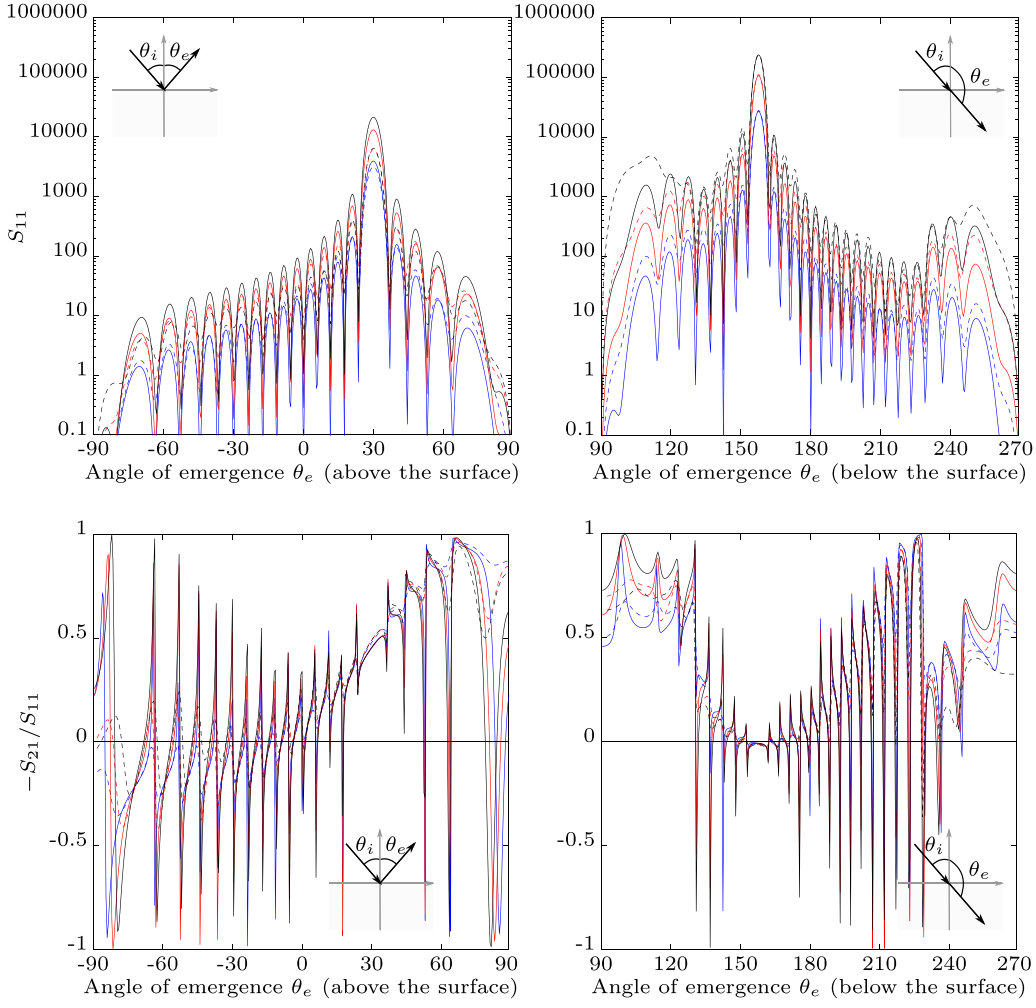

Fig. 12. As in Fig. 11, but with incident light propagating in the xz-plane from above the surface at a 30° angle with respect to the z-axis and excluding azimuthal averaging.

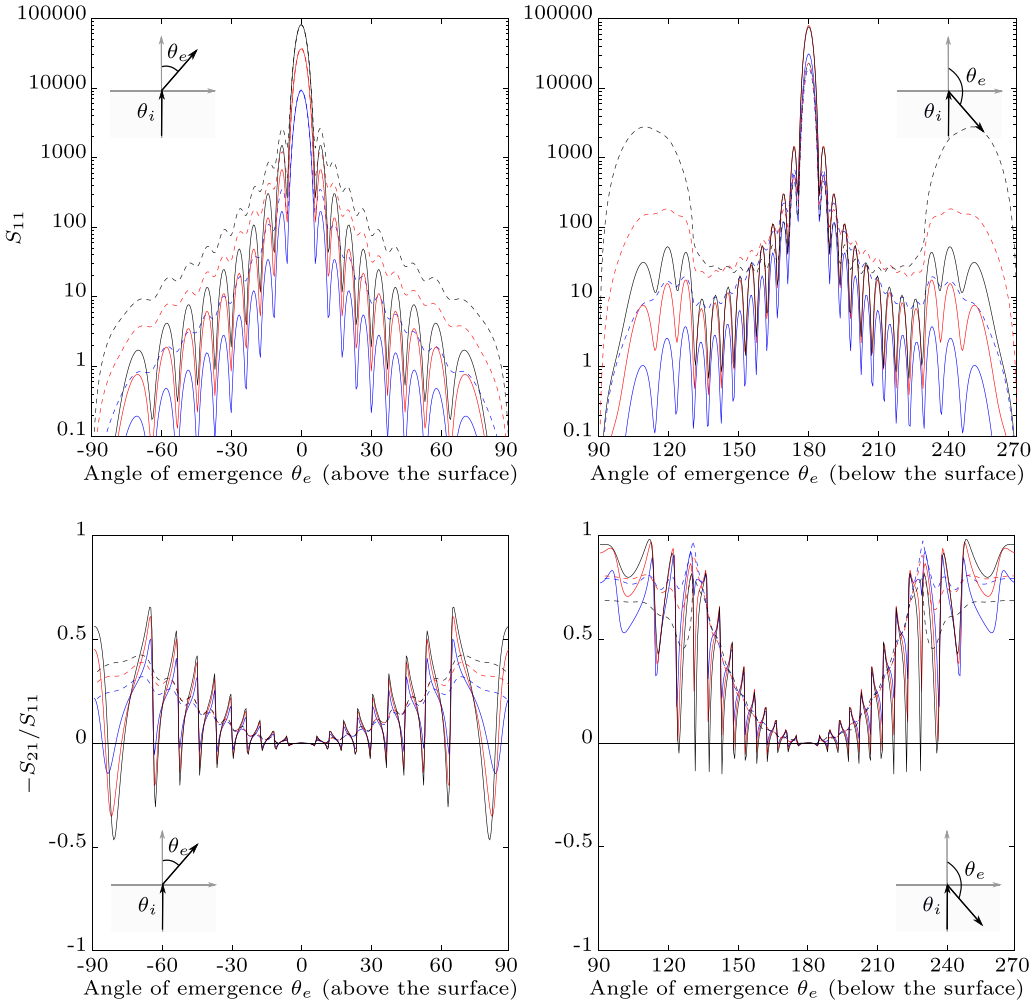

Fig. 13. As in Fig. 11, but with incident light propagating in the *xz*-plane from below the surface along the *z*-axis. Results are averaged over the azimuth angle ϕ.

Values for the roughness parameters were selected after literature and sensitivity studies. The Hurst exponent values found in the literature are, e.g., $H = 0.3, 0.5,$ and 0.7 [42], $H = 0.2, 0.5,$ and 0.8 [38] or $H = 0.25, 0.375, 0.5, 0.625,$ and 0.9 [26]. After initial testing, $H = 0.3, 0.5,$ and 0.7 were chosen through visual inspection, as the aim was to simulate the ice crystal surfaces as realistically as possible. The more extreme values of H resulted in surfaces that did not resemble the images of the rough ice crystal surfaces seen in the literature [11,13,15,16].

The root-mean-square roughness values chosen were based on the literature study in Section 1. The morphological features seen in the SEM images of ice crystal surfaces were of the scale of 0.1 to 20 µm, the larger scale denoting the separations between the strands seen in the crystals [13–15]. Several experiments with ADDA simulations were performed using surface-roughness elements generated with different values of R_q, and $R_q = 0.05, 0.1,$ and 0.15 µm were chosen for further studies. Due to computational limitations, it was not possible to simulate different roughness scales by using tenfold values of R_q compared to the observed roughness scale of 0.1 µm, such as 0.01, 0.1, and 1 µm, as the dipole size d required to describe the surfaces with the smallest R_q accurately (see Section 2.3) resulted in too large total dipole numbers for the simulations with the largest R_q.

Nine combinations of H and R_q were studied, with ten surface realizations generated for each H, R_q-pair. The maximum height of an element z_{max} was kept constant for each set of elements. This allowed the height from the surface h_s defined in Eq. (18) to be kept constant for each H, R_q - combination. In total, 90 different elements were generated. Examples of the two-dimensional surface height profiles generated with the H, R_q - combinations studied are shown in Fig. 6, and sample rough surfaces in Fig. 7.

3.2. Experimenting with ADDA-S

Before studying the scattering by the surface-roughness elements with different roughness parameters, initial testing was carried out. First, different shapes for the base of the elements were tested by cutting a circular portion of the square-based surface elements. Based on the scattering computations performed for the circular and rectangular surface elements, the shape of the base did not significantly affect the results. Therefore, a square base was used for the final computations.

The differences due to the surface realizations were studied by generating ten surfaces with roughness parameters $H = 0.5$ and $R_q = 0.1$ µm. The scattered intensity S_{11} and the degree of linear polarization $-S_{21}/S_{11}$ for unpolarized incident light were computed for the ten surfaces, along with S_{11} and $-S_{21}/S_{11}$ averaged over the different surface realizations. Results for incident light propagating in the *xz*-plane from above the surface along the *z*-axis are presented in Fig. 8, and from below the surface at a 30° angle with respect to the *z*-axis in Fig. 9.

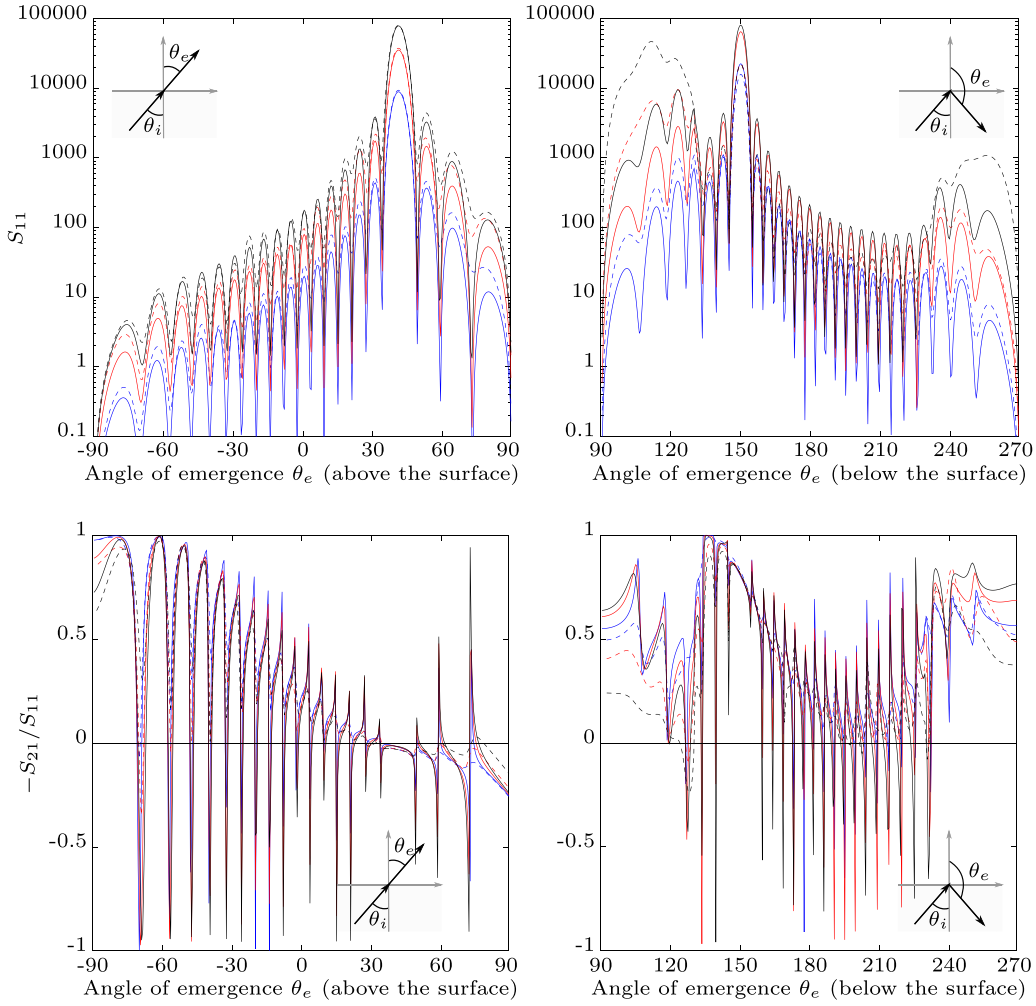

Fig. 14. As in Fig. 11, but with incident light propagating in the *xz*-plane from below the surface at a 30° angle with respect to the *z*-axis and excluding azimuthal averaging.

Averaging over the azimuth angle ϕ was only possible when the incident light was propagating in the direction of the normal of the surface (along the *z*-axis). To test the dependence of scattering quantities on ϕ, the scattered intensity S_{11} and the degree of linear polarization $-S_{21}/S_{11}$ were computed for values of $\phi = 0°$ to $\phi = 90°$ in 10° increments (Fig. 10). Here, incident light was propagating in the *xz*-plane, from above the surface at a 30° angle with respect to the *z*-axis. Surface-roughness elements with roughness parameters $H = 0.5$ and $R_q = 0.1\,\mu m$ were used for this case, and the results were averaged over ten surface realizations.

3.3. Rough and smooth elements

Scattering by smooth and rough elements was compared by generating rectangular smooth elements with a total number of dipoles N comparable to the corresponding rough elements. As R_q was found to be the dominating factor for N, the average N of each set of elements with the same R_q was chosen to determine the size of the smooth elements (see Table 1). A square base with an edge length of 5 µm and the same dipole size $d = 4.9\,nm$ as for the rough elements was used to generate the smooth elements. For the scattering calculations, rough elements with the Hurst exponent $H = 0.5$ were studied along with the smooth elements. The scattering results of the rough elements were averaged over ten surface realizations for each R_q. Scattered intensity S_{11} and degree of linear polarization $-S_{21}/S_{11}$ for the rough and smooth elements with four different incident light directions are presented in Figs. 11–14.

3.4. Effect of the roughness parameters R_q and H

Finally, the effect of the roughness parameters on light scattering from the surface-roughness elements located near a plane surface has been studied by calculating the scattered intensity S_{11} and degree of linear polarization $-S_{21}/S_{11}$ for the rough elements generated with all H, R_q - combinations specified in Section 3.1. As orientation averaging has not been available for ADDA-S, several individual incident light propagation directions have been used in the study. Incident light is propagating in the *xz*-plane from directly above or below the surface, and at 15° and 30° angles with respect to the *z*-axis for both above and below the surface. Results are shown in Figs. 15–20.

4. Discussion

Results of the light scattering computations presented in Section 3 are rich in differences and details; therefore, the main results are analysed collectively in this section.

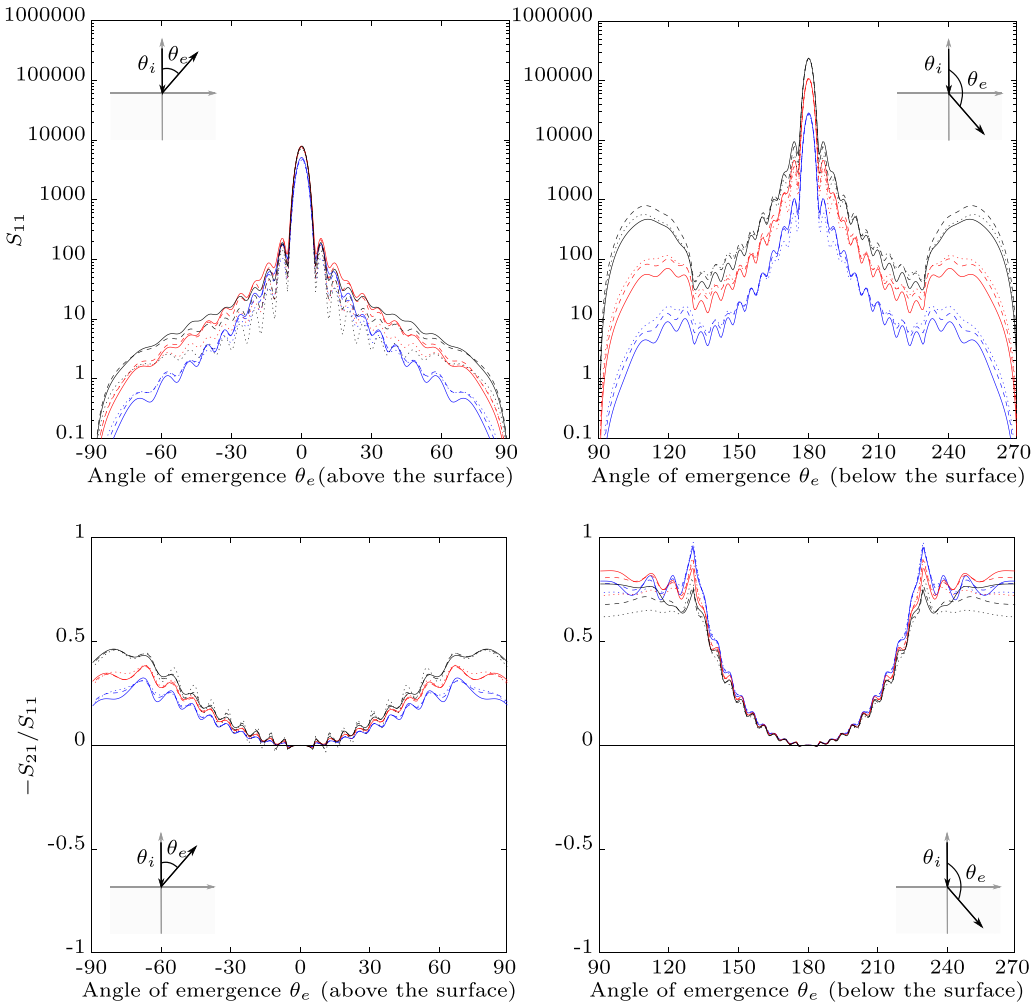

Fig. 15. Scattered intensity S_{11} and the degree of linear polarization $-S_{21}/S_{11}$ for unpolarized incident light above the surface (left) and below the surface (right). Different combinations of roughness parameters are indicated by $R_q = 0.05\,\mu m$ (blue), 0.1 μm (red), and $0.15\,\mu m$ (black), and $H = 0.3$ (solid line), 0.5 (dashed line), and 0.7 (dotted line). Incident light is propagating in the xz-plane from above the surface along the z-axis. Results have been averaged over the azimuth angle ϕ. Values of $S_{11} < 0.1$ have been omitted for illustrative purposes.

Little difference between individual surface-roughness realizations can be seen for both the scattered intensity S_{11} and the degree of linear polarization $-S_{21}/S_{11}$, when the incident light is propagating along the surface normal from above (Fig. 8). The differences are greatly increased as the incident light propagates at a 30° angle with respect to the surface normal from below (Fig. 9). In the latter case, while the averaged $-S_{21}/S_{11}$ reflected below the surface is positive for nearly all θ_e, individual surfaces show both positive and negative polarization with large variation. A similar effect is visible for $-S_{21}/S_{11}$ transmitted above the surface. However, even though some of the individual surface-roughness elements have much larger polarizations (or even of the opposite sign) than the average $-S_{21}/S_{11}$, the angular distributions follow a similar trend. The effect of individual surface-roughness elements could be further diminished by averaging over a larger number of realizations, thus achieving statistically more meaningful results especially for incident light directions other than those normal to the surface.

Fig. 8 shows interference maxima and minima for S_{11} and $-S_{21}/S_{11}$ both above the surface and below the surface. The half-edge-length size parameter is ∼30 for the current vacuum wavelength, in agreement with the number of extrema above the surface. Below the surface, the extrema are narrower and their number is larger, consistent with the shorter wavelength inside the material. The S_{11} value for the specularly reflected light is an order of magnitude weaker than the corresponding peak for the specularly transmitted light which is again consistent. For transmitted light, there are clearly two distinct angular regimes dictated by the maximum refraction angle into the ice material, that is, the limiting total internal reflection angle. Although this term is widely known as a purely geometric optics concept, it is here used for convenience and in alignment with previous work, e.g., [34], who discuss the optical counterpart of the so-called Yoneda peak [32]. For the vacuum-ice interface, this angle is 49° and results in sharp boundaries at around 229° and 131° in Fig. 8 for the scattering patterns below the surface. In the refraction-type domain from 180° to the aforedescribed angles, the intensity drops, whereas, beyond these angles, there is a sudden increase. Polarization at reflection is increasingly positive with increasing angular distance from the exact backscattering direction, yet another consistent feature in the scattering characteristics. Polarization at transmission is no longer negative as in Fresnel refraction: it is positive essentially everywhere, an important new result. The high values of polarization near 131° and 229° coincide with the ends of the angular domain of refraction into the material. The exact backscattering direction coincides with the

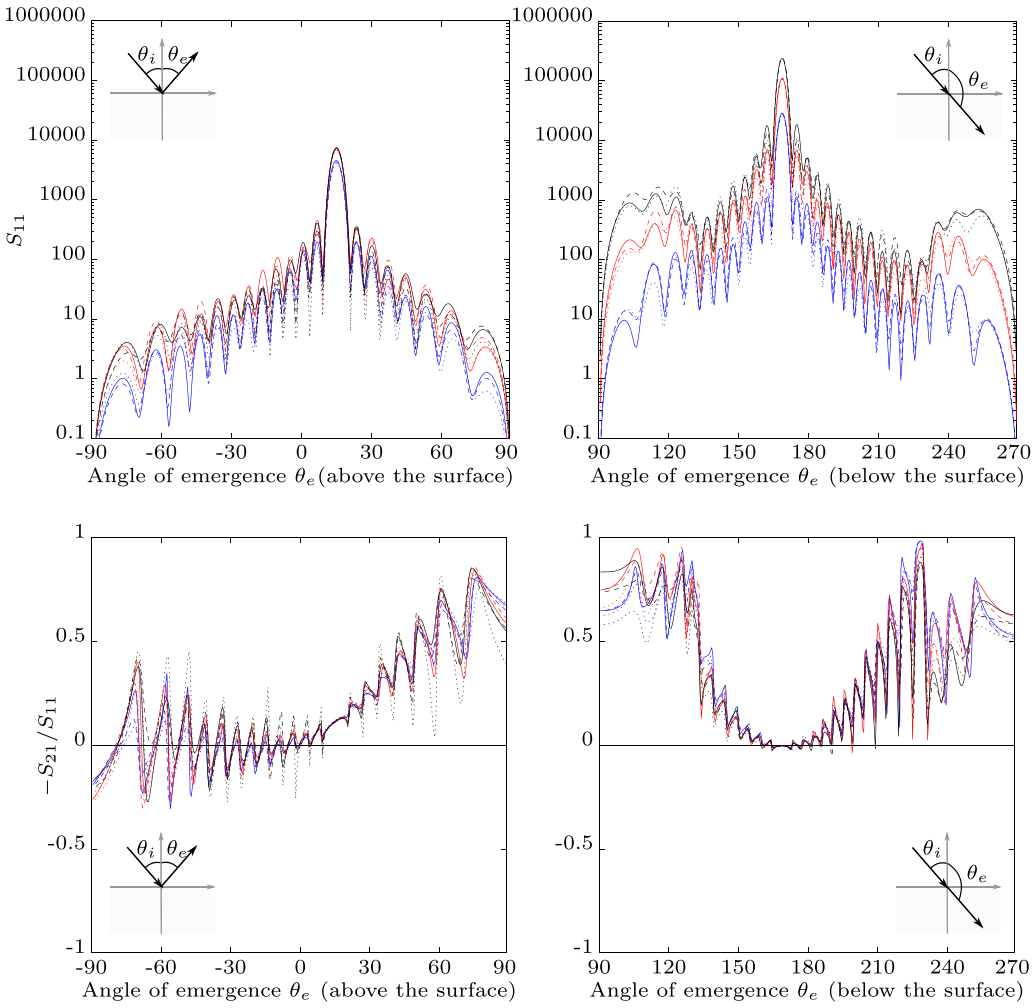

Fig. 16. As in Fig. 15, but with incident light propagating in the *xz*-plane from above the surface at a 15° angle with respect to the *z*-axis and excluding azimuthal averaging.

direction of specular reflection, and it is hard if not impossible to resolve between the coherent backscattering and specular contributions.

In Fig. 9, even though the incidence is from below, there are several features similar to those in Fig. 8. Strong internal reflection from parts of the surface-roughness element, a precursor to total internal reflection in the case of infinite plane boundaries between two media, is likely to play an important role. In particular, what we term the strong internal reflection mechanism is in agreement with the lower polarization for angles less than 120° below the surface. Above the surface, positive polarization increasing toward −90° can derive from diffuse scattering by the features of the surface-roughness elements. Below the surface, positive polarization for $> 240°$ deg is consistent with diffuse scattering by surface features.

For different values of the azimuth angle ϕ, with light incident from above, the largest scattered intensity is found at $\phi = 0°$ (Fig. 10). As $\phi \to 90°$, the angular distributions for both scattered intensity S_{11} and degree of linear polarization $-S_{21}/S_{11}$ for unpolarized incident light are smoothened, and S_{11} is significantly reduced (up to 10^3 less than the values for $\phi = 0°$). Also, the peaks in the angular distribution of S_{11} for specular reflection above the surface and S_{11} refracted below the surface diminish, and the angle for the largest S_{11} is shifted towards $\theta_e = 0°$ and 180° for above and below the surface, respectively. Polarization becomes positive with increasing ϕ, especially for reflected light.

Fig. 10 shows no retroreflection peak due to double external reflection from the 90° trough at −30°: the reason is likely to be the small height of the vertical side as compared to the wavelength. There is clear symmetry for the case of 90° azimuth angle. Below the surface, lower polarization for $> 230°$ than for $< 130°$ can be due to the increased proportion of diffuse scattering for the former case. Above the surface, the same effect can be seen for $< 0°$.

Smooth elements reflect more light when the incident light is propagating along the surface normal, while rough elements have a larger proportion of the intensity transmitted through the surface (Figs. 11 and 13). The largest peak for S_{11} is close to equal for both smooth and rough elements. For incident light propagating along the surface normal, the rough elements have only positive polarization and a relatively featureless angular distribution of polarization with a minimum at $\theta_e = 0°$ and 180°, whereas their smooth counterparts show a rapidly changing pattern in the polarization, reaching even negative values.

Much less difference for both S_{11} and $-S_{21}/S_{11}$ between the rough and smooth elements is found for incident light propagating at a 30° angle with respect to the surface normal, although the variation in S_{11} and $-S_{21}/S_{11}$ is larger for the smooth elements (Figs. 12 and 14). For the case with incident light com-

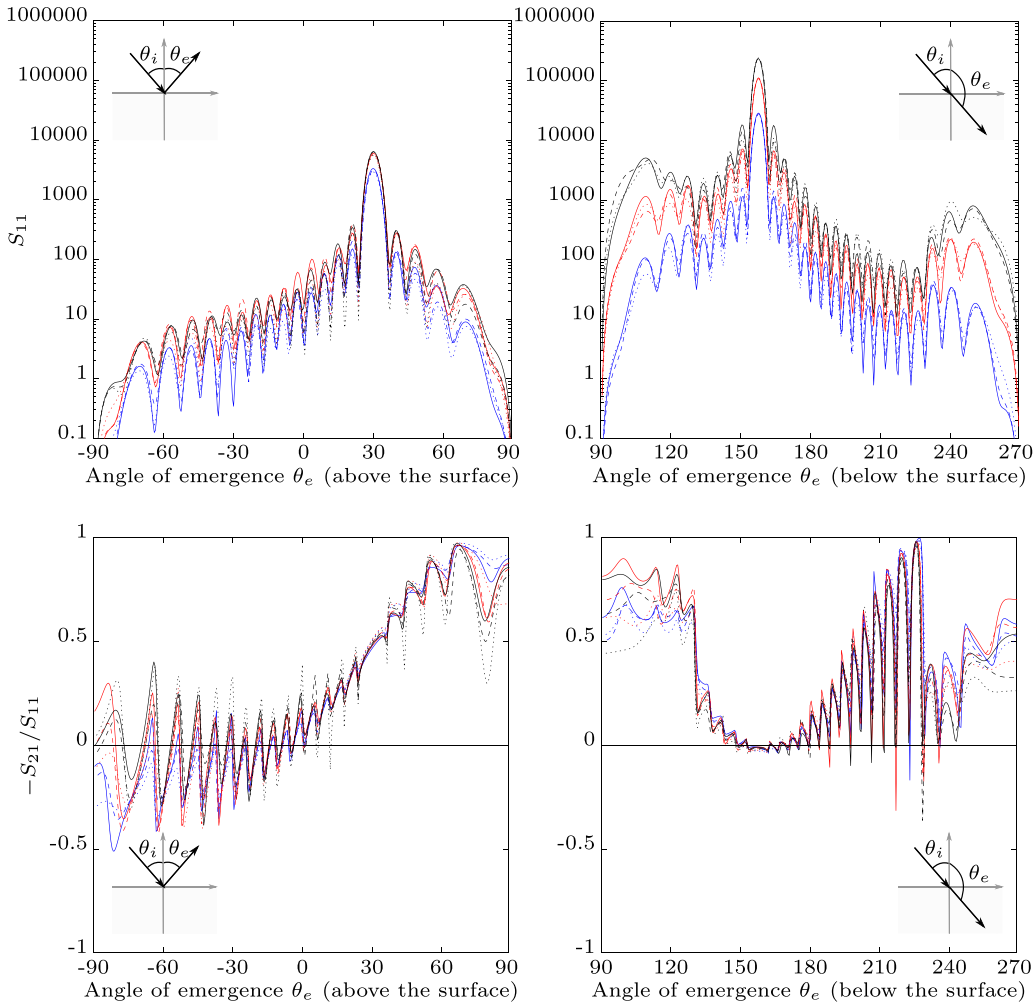

Fig. 17. As in Fig. 15, but with incident light propagating in the *xz*-plane from above the surface at a 30° angle with respect to the *z*-axis and excluding azimuthal averaging.

ing from below the surface at a 30° angle, the completely linearly polarized peak where $-S_{21}/S_{11} = 1$ is visible for all smooth cases around the Brewster angle ([41], see also [34]) which, for the ice-air boundary, is $\sim 37°$. When considering the results from the smooth elements, it should be noted that they, too, are composed of dipoles, and therefore are not smooth in a sense similar to, e.g., a boundary between two media in geometric optics models.

The rougher the element (larger values of the vertical roughness parameter R_q and smaller values of the horizontal roughness parameter H), the more of the scattered intensity is transmitted through the plane surface, whereas the smoother elements reflect more light (Figs. 15–20). This is in agreement with the previous results discussed in Section 1. For S_{11} corresponding to transmission through the surface, there is little dependence for the horizontal roughness parameter H (except that the rougher elements refract more light through the plane boundary). However, the angular distribution of the reflected intensity S_{11} has a larger variation for different values of H at roughly $\pm 30°$ around the specular reflection maximum in S_{11}. This effect is most notable for the largest R_q.

For S_{11} corresponding to reflection, there are higher intensity values for $R_q = 0.1\,\mu m$ regardless of the incident light direction, in contrast of the expected result of the highest values of S_{11} for largest R_q. This may be due to a resonance effect, e.g., due to $R_q = 0.1\,\mu m$ being one fifth of the wavelength of the incident light.

While the angular distribution of degree of linear polarization is smoothened with surface roughness, the roughness parameters R_q and H were not found to affect the polarization. Therefore, roughness itself affects polarization, but the exact surface morphology does not seem to have a significant effect.

Prominent peaks in scattered intensity are seen in all the cases of S_{11} below the surface within specific angular ranges ($\theta_e = 90° - 130°$ and $230° - 270°$). The angular characteristics of these peaks do not depend on the direction of the incident light, or the roughness parameters. The peaks are higher for surface elements with larger R_q, but the value of the Hurst exponent H corresponding to the highest peaks varies with the incident angle θ_i. For different values of ϕ, the peaks become relatively more prominent as $\phi \to 90°$ and the overall scattered intensity decreases. In addition, the rough elements have higher peaks than their smooth counterparts. As the element studied here is finite, the size of the element may affect the results. A finite surface-roughness element affects scattering by reducing the angular resolution of the scattered fields, and by causing effects from the surface edges (Maradudin [27], p. 185). Consideration of angular resolution with respect to surface size might be needed, as well as removing effects caused by surface edges

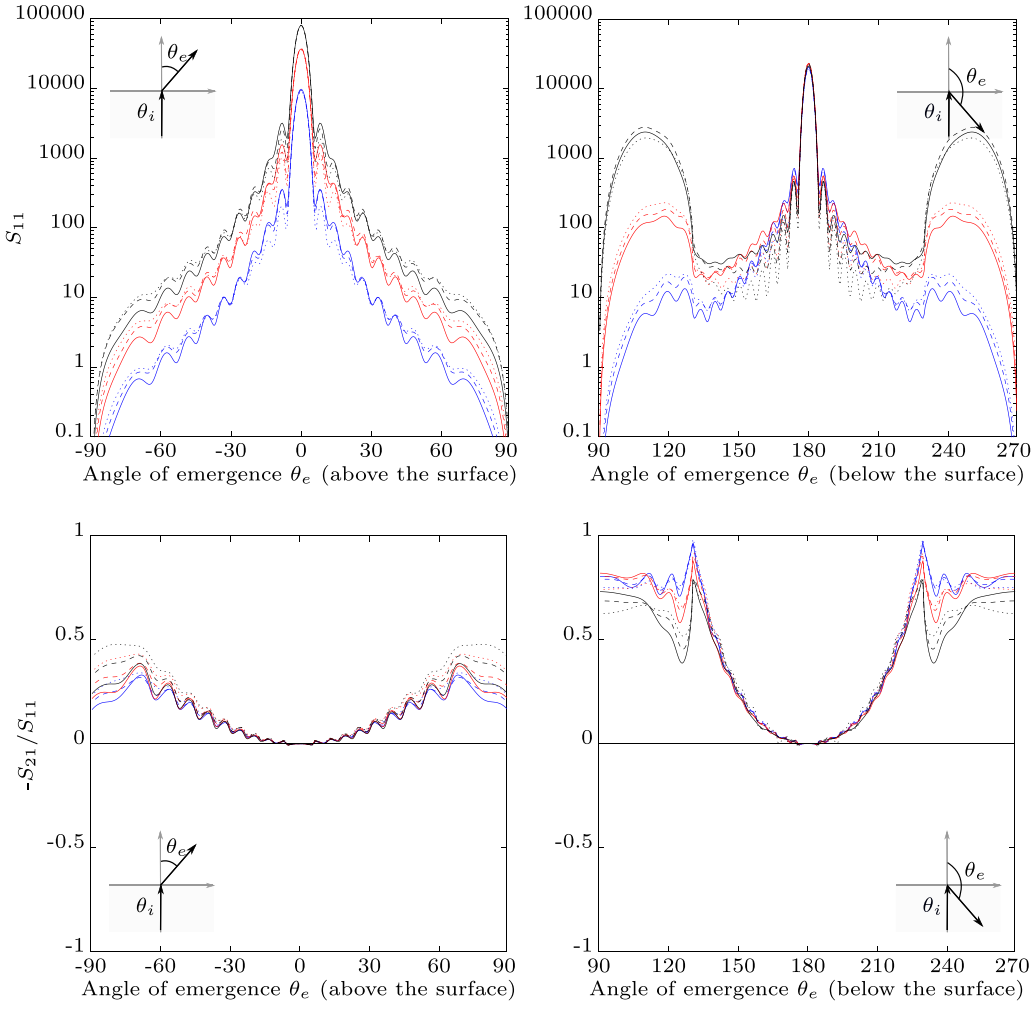

Fig. 18. As in Fig. 15, but with incident light propagating in the *xz*-plane from below the surface along the *z*-axis. Results are averaged over the azimuth angle ϕ.

by, e.g., reducing the intensity of the incident field on surface edges (see [27], Ch. 7 and references therein). A larger surface-roughness element could not be studied here due to computational limitations.

Strong internal reflection from parts of the surface-roughness element is identified as a potential explanation for the scattering phenomena observed below the surface outside the refraction domain. These phenomena show up, ubiquitously, as shoulders in S_{11} in Figs. 8–20, as well as in degrees of polarization $-S_{21}/S_{11}$ as case-by-case agreement with the strong internal reflection mechanism. It is important to notice that, due to the finite size of the element and its parts, the mechanism is strictly a precursor to the conventional total internal reflection mechanism. Diffraction plays an important, additional role in transforming the surface fields into scattered fields at infinity, resulting in extended angular ranges for the phenomena, even in shoulders for smooth elements. Note that there is little or no interference structure in the shoulders for the rough elements but that there is pronounced interference structure for the smooth elements: the smoothening is evidently due to the fact that contributions are accrued from the entire area of the elements with varying effective sizes of its contributing parts.

Strong internal reflection is important when light is incident from above and from below. In the former case, recalling Eq. (14), the incoming field consists of the incident as well as the reflected field components. It is now the reflected field that gives rise to strong internal reflection. In the latter case, the incoming field is solely the field transmitted through the infinite boundary. Since the reflected field is significantly weaker than the transmitted field, one expects stronger shoulders for the cases, where light is incident from below. This is indeed clear from Figs. 8–20. In particular, the shoulder strengths are considerably different in Figs. 11 and 13 as well as in Figs. 15 and 18. Figs. 17 and 20 show the shoulders for oblique incidence from above and below, respectively. Now the shoulders are asymmetric and in agreement with enhanced internal reflection in directions indicated by the incident direction (positive dot product between vectors; from now on, positive direction) and subdued internal reflection in directions opposite to the incident direction (negative direction). In Fig. 20, for the roughest element, the shoulder is even stronger than the specular reflection peak.

Consider next the polarization phenomena in $-S_{21}/S_{11}$ accompanying the shoulders in S_{11}, starting from the case of light incident from above the surface. In Fig. 8, the high positive polarization is due to the further internal reflection of the reflected component of the incident field. Fig. 10 shows similar polarization in the positive direction, whereas, in the negative direction, the polarization is clearly neutralized due to the smaller angle

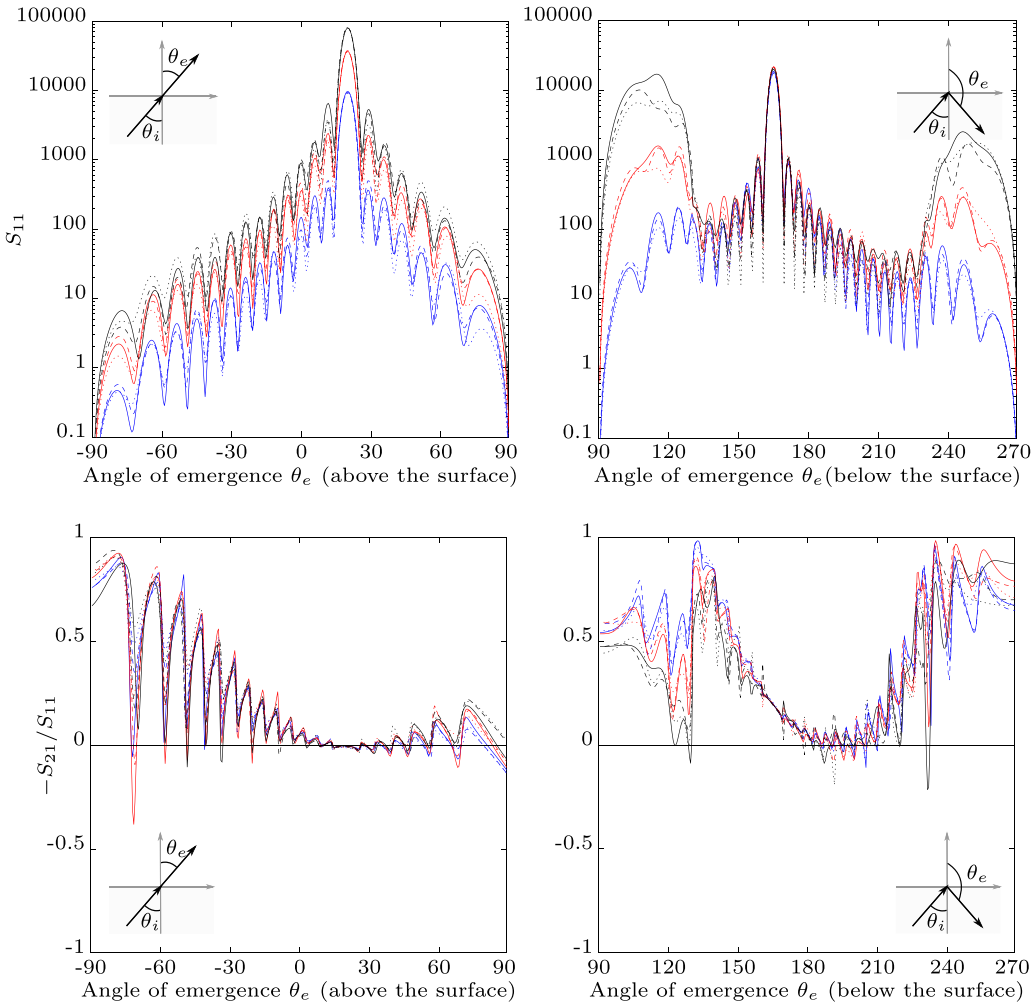

Fig. 19. As in Fig. 15, but with incident light propagating in the *xz*-plane from below the surface at a 15° angle with respect to the *z*-axis and excluding azimuthal averaging.

of incidence for the internal reflection. The sideways polarization is high, potentially due to a decreased amount of diffuse scattering from the rough features. Figs. 11, 12, and 15–17 show similar phenomena in agreement with the strong internal reflection mechanism.

In the case of light incident from below, polarization phenomena are again consistent with the strong internal reflection mechanism. In Fig. 9, in the positive direction, the polarization is low due to the largely unpolarized incident field experiencing total internal reflection on the surface-roughness element. In the negative direction, the polarization is higher due to the normal internal reflection polarizing the incident light positively. In a similar way, one can explain the polarization patterns in Figs. 13, 14, and 18–20.

Ermutlu et al. [56] (see also [30,31]) have found similar peaks in scattering by a single electric dipole particle below an infinite, smooth interface between two materials. In their case, the peaks are likely to be caused by total internal reflection on the interface. The peaks show interference structure depending on the distance of particle from the interface. Indeed, it is also possible to explain the shoulders (see above) using total internal reflection on the vacuum-ice boundary by a higher-order interaction between the surface-roughness element, the icy material near the element below the interface, and the infinite plane boundary surrounding the surface-roughness element. We note that Total Internal Reflection Spectroscopy (see, e.g., [57]) relies on the effect of scatterers located above an interface on the scattered waves in the medium below the interface. In their cases, the shoulder phenomenon is not as pronounced as in the present case, but the origin of the phenomenon is the same. The shoulders have been briefly mentioned in Hetland et al. [34] with conclusion that they were not connected to the Yoneda peak.

Finally, Yurkin and Huntemann [51] point out that certain inconsistencies exist in ADDA-S for the internal fields in the case of absorbing materials. We note that the ice material is here assumed to be weakly absorbing so that, strictly, the scattered fields inside the material must vanish at infinity. However, due to the minute imaginary part of the refractive index, we expect that the present results are an accurate proxy for the case of non-absorbing ice material. We recall that the edge length of the surface-roughness elements is presently precisely ten times the vacuum wavelength which may well bear on the detailed interpretation of the scattering characteristics. Nevertheless, we expect that the present study does bring up the key scattering characteristics of rough vacuum-ice interfaces.

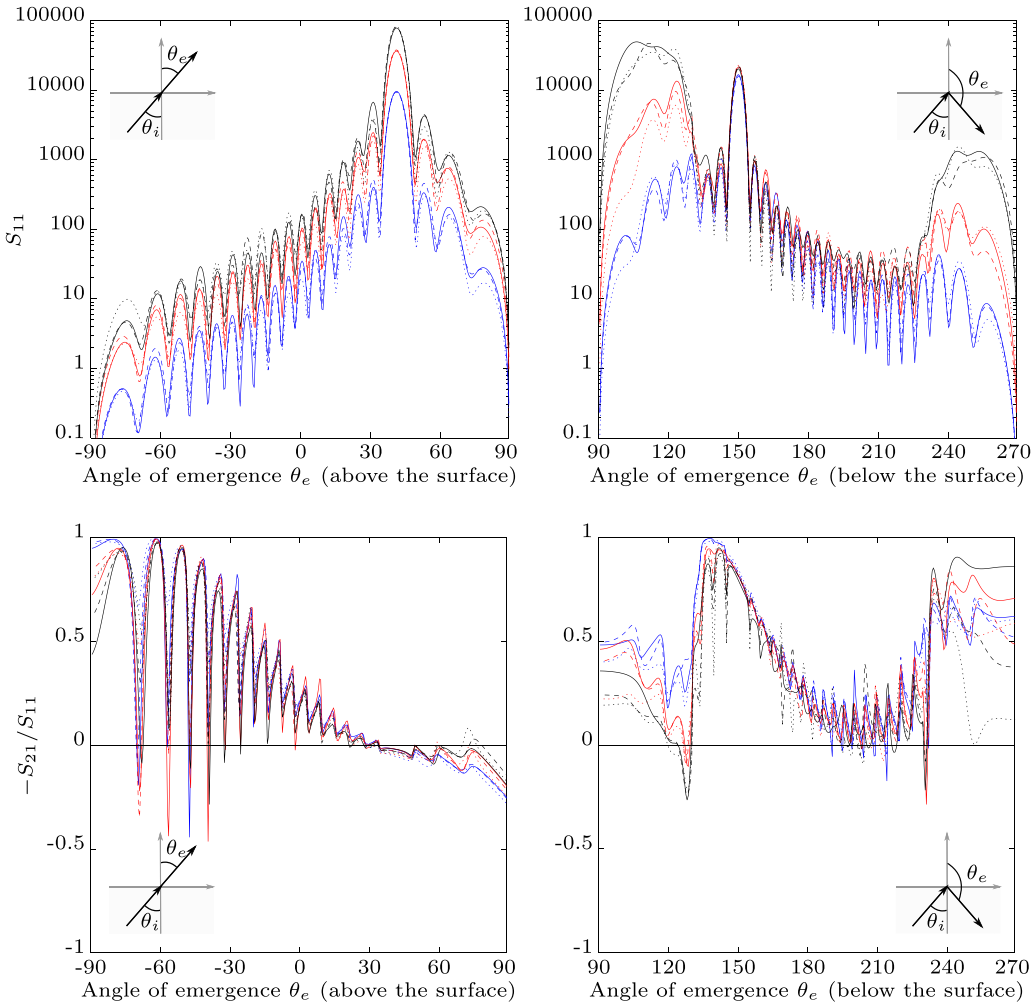

Fig. 20. As in Fig. 15, but with incident light propagating in the *xz*-plane from below the surface at a 30° angle with respect to the *z*-axis and excluding azimuthal averaging.

5. Conclusions

Light scattering by ice crystals has many applications in atmospheric physics from the interpretation of optical measurements to the radiative transfer computations needed for remote sensing and climate simulations. Surface roughness is an important yet inadequately quantified factor in scattering by atmospheric ice crystals. While the presence of surface roughness is known to smooth out the features on the angular patterns of scattered intensity and polarization as compared to those for smooth crystals, the morphology of ice crystal surfaces found in nature is not known, nor how roughness depends on atmospheric conditions.

A new method for computing scattering by rough ice crystal surfaces has here been developed by investigating a finite, thin surface-roughness element on top of a planar ice surface. The element has been generated using a model deriving from fractional Brownian motion, where surface morphology is determined by the vertical and horizontal roughness parameters R_q and H. Light scattering computations have been performed with ADDA-S for an ensemble of surface-roughness elements created with different roughness parameters, along with smooth elements for comparison.

For the limited amount of cases studied, smooth elements are shown to reflect more light than rough elements. In addition, based on our results, the rougher the element is, the more scattered light is transmitted through the planar surface. These results should not, however, be generalized without precaution; for example, previous DDA simulations for rough ice crystals show non-systematic changes and that the effect may be dependent on the size parameter or the scale of roughness [25]. The angular distribution of the degree of linear polarization is smoother for rough elements compared to smooth elements, but the roughness morphology does not have a considerable effect on polarization. The vertical roughness parameter R_q dictates how much light is transmitted through the surface, while the horizontal roughness parameter H affects the angular distribution of scattered light. For light scattered below the surface, peaks in scattered intensity are seen in a specific angular region ($\theta_e = 90^\circ - 130^\circ$ and $230^\circ - 270^\circ$). The effect is present for all incident light propagation directions, and is more prominent with increasing roughness. The effect is, at least to a large part, a manifestation of strong internal reflection on the element boundary, either by the reflected part of the incoming field, when light is incident from the vacuum above, or by the transmitted field, when light is incident from the ice material below. Diffraction due to the finite size of the surface element further affects the angular dependences at infinity. We note that the present work underscores the significance of near-surface scattering waves for arbitrary, localized surface deformations on ice crystal faces. In a future study, we plan to study the effect of the thickness of the surface roughness element on the scattering characteristics.

Realistic representations of rough ice crystal surfaces could in principle be generated with the present surface-roughness model by first developing a method for retrieving the corresponding

roughness parameters from the surface measurements. For instance, SEM imaging [16,17] or ice analogue particles [25] could be used. It should be noted that retrieving ice crystal surfaces from the SEM images depends on the resolution and magnification of the microscope, and orientation of the crystal with respect to the viewing angle [15]. Therefore, surface height profiles could be over- or underestimated due to measurement errors. In addition, naturally-occurring atmospheric ice crystals may have surface structures different from those grown inside microscope chambers. Based on the scattering computations performed, for applications such as climate models where the information of ice cloud reflectivity is essential, it may be sufficient to know the vertical scale of the surface roughness to develop a model for rough ice crystal surfaces. For a more thorough analysis on how the surface-roughness elements scatter light, also the horizontal roughness scale is needed, as it was shown to affect the angular dependence of S_{11}. The direction of the scattered light is needed for, e.g., more complex ice crystal habits, where light scattered from the rough surface may encounter yet another crystal facet.

Additional improvements on the computations performed could be achieved by further development of ADDA-S. Especially the restrictions to the particle size (regardless of the total number of dipoles) caused limitations in the computations. Roughness on smaller scales could result in different effects on scattered quantities, but these computations would require a reduction in dipole size. However, there is currently no evidence of nano-scale surface roughness, as even the SEM images have limited resolution (see Section 1). Therefore, more information on the surfaces of ice crystals is needed. In addition to SEM imaging, information on a rough surface can be obtained indirectly by the inverse scattering problem, i.e., deducing the rough surface profile from the scattered field (see [27], Ch. 16). Another further investigation would be scatterers that are partially submerged in the surface. This could provide more realistic models of surface roughness with the addition of scratches and dents in the surface of the ice crystal. Incorporating confined, Gaussian beams as incident light can open up interesting pathways to the interpretation of the scattering characteristics presently documented.

Whereas the present scattering results and the rough surface model developed can be used in a multitude of applications including light scattering by atmospheric particles other than ice crystals, the problem of solving light scattering by large ice crystals (size parameter $x > 100$) with surface roughness is still unresolved. Ultimately, further advances could be achieved by combining the model used here with a geometric optics model (e.g., in Muinonen et al. [58]). As the amplitude scattering matrix is given by ADDA-S, the information of the fields scattered by the surface-roughness element is available. With suitable interpolation, the scattered field could be incorporated into a geometric optics model, combining the ability of geometric optics to compute scattering by large particles to the small-scale features caused by surface roughness solvable with ADDA-S. The surface-roughness element represents the roughness on an ice crystal, while ADDA-S takes into account the effect of the large ice crystal on the surface computations. Geometric optics could then solve the reflections and refractions of light in the large ice crystal. However, additional work is required, as effects caused by the edges of the surface element need further consideration. Also, incident light cannot propagate parallel to the plane surface, and it is expected that some effects caused by the surface would arise for angles near 90° with respect to the surface normal.

The model for light scattering by a rough surface used here can be applied to other wavelengths or surface roughness size scales, although a different model for scattering computations may be needed, as discretizing larger surfaces for ADDA-S will result in total number of dipoles too large for the present computational resources. However, further development is needed before the results obtained here for ice crystals with surface roughness can be used in applications such as remote sensing. The fractal surface model (Section 2.2) in itself is useful for many applications for light scattering by rough surfaces, and, as it is scale-invariant, it can be applied to many different wavelengths and spatial scales. Examples include sunlight scattered by mineral dust particles, microwave radiation reflected from snow-covered ground, and light scattering from atmosphereless solar system bodies such as asteroids, cometary nuclei, Mercury, and the Moon.

Declaration of Competing Interest

The authors declare that they have no known competing financial interests or personal relationships that could have appeared to influence the work reported in this paper.

CRediT authorship contribution statement

Elina Riskilä: Methodology, Validation, Formal analysis, Investigation, Resources, Data curation, Writing - original draft, Writing - review & editing, Visualization. **Hannakaisa Lindqvist:** Conceptualization, Formal analysis, Investigation, Writing - review & editing, Supervision. **Karri Muinonen:** Conceptualization, Formal analysis, Investigation, Writing - review & editing, Supervision.

Acknowledgements

Research has been partially funded by the Academy of Finland (Projects 285421, 298137, and 325805). Dr. Maxim Yurkin is acknowledged for making his ADDA code publicly available. We thank the two anonymous reviewers for their constructive comments.

Supplementary material

Supplementary material associated with this article can be found, in the online version, at doi:10.1016/j.jqsrt.2021.107561.

References

[1] Yang P, Kattawar G, Hong G, Minnis P, Hu Y. Uncertainties associated with the surface texture of ice particles in satellite-based retrieval of cirrus clouds—Part II: effect of particle surface roughness on retrieved cloud optical thickness and effective particle size. IEEE Trans Geosci Remote Sens 2008;46(7):1940–7.
[2] Rolland P, Liou K-N, King MD, Tsay S, McFarquhar G. Remote sensing of optical and microphysical properties of cirrus clouds using modis channels: Methodology and sensitivity to assumptions. J Geophys Res 2000;105(D9):11721–38.
[3] IPCC. Climate change 2013: The physical science basis. IPCC Working Group I Contribution to AR52013;Ch. 7: Clouds and aerosols.
[4] Baran A. From the single-scattering properties of ice crystals to climate prediction: a way forward. Atmos Res 2012;112:45–69.
[5] Lindqvist H, Muinonen K, Nousiainen T, Um J, McFarquhar G, Haapanala P, et al. Ice-cloud particle habit classification using principal components. J Geophys Res 2012;117:D16206.
[6] Macke A, Mueller J, Raschke E. Single scattering properties of atmospheric ice crystals. J Atmos Sci 1996;53(19):2813–25.
[7] Yang P, Liou K-N. Single-scattering properties of complex ice crystals in terrestrial atmosphere. Control Atmos Phys 1998;71(2):32–63.
[8] Yang P, Bi L, Baum B, Liou K-N, Kattawar G, Mischenko M, et al. Spectrally consistent scattering, absorption, and polarization properties of atmospheric ice crystals at wavelengths from 0.2 to 100 µm. J Atmos Sci 2013;70:330–47.
[9] Schmitt C, Heymsfield A. On the occurrence of hollow bullet rosette and column-shaped ice crystals in midlatitude cirrus. J Atmos Sci 2007;64:4514–19.
[10] Schnaiter M, Järvinen E, Vochezer P, Abdelmonem A, Wagner R, Jourdan O, et al. Cloud chamber experiments on the origin of ice crystal complexity in cirrus clouds. Atmos Chem Phys 2016;16:5091–110.
[11] Ulanowski Z, Kaye P, Hirst E, Greenaway R, Cotton R, Hesse E, et al. Incidence of rough and irregular atmospheric ice particles from small ice detector 3 measurements. Atmos Chem Phys 2014;14:1649–62.
[12] Cole B, Yang P, Baum B, Riedi J, Labonnote L. Ice particle habit and surface roughness derived from PARASOL polarization measurements. Atmos Chem Phys 2014;14:3739–50.

[13] Pfalzgraff W, Hulscher R, Neshyba S. Scanning electron microscopy and molecular dynamics of surfaces of growing and ablating hexagonal ice crystals. Atmos Chem Phys 2010;10:2927–35.
[14] Neshyba S, Lowen B, Benning M, Lawson A, Rowe P. Roughness metrics of prismatic facets of ice. J Geophys Res 2013;118:1–10.
[15] Magee N, Miller A, Amaral M, Cumiskey A. Mesoscopic surface roughness of ice crystals pervasive across a wide range of ice crystal conditions. Atmos Chem Phys 2014;14. 12371–12357
[16] Butterfield N, Rowe P, Stewart E, Roesel D, Neshyba S. Quantitative three-dimensional ice roughness from scanning electron microscopy. J Geophys Res Atmos 2017;122:3023–41.
[17] Magee N, Boaggio K, Staskiewicz S, Lynn A, Zhao X, Tusay N, et al. Captured cirrus ice particles in high definition. Atmos Chem Phys Discuss 2020;2020:1–27. doi:10.5194/acp-2020-486.
[18] Lindqvist H, Martikainen J, Räbinä J, Penttilä A, Muinonen K. Ray optics in absorbing media with application to ice crystals at near-infrared wavelengths. J Quant Spectrosc Radiat Transf 2018;217:329–37.
[19] Yang P, Liou K-N, Bi L, Liu C, Yi B, Baum B. On the radiative properties of ice clouds: light scattering, remote sensing, and radiation parametrization. Adv Atmos Sci 2015;32:32–63.
[20] Tang G, Panetta R, Yang P, Kattawar G, Zhai P-W. Effects of ice crystal surface roughness and air bubble inclusions on cirrus cloud radiative properties from remote sensing perspective.. J Quant Spectrosc Radiat Transf 2017;195:119–31.
[21] Shcherbakov V. Why the 46° halo is seen less than the 22° halo? J Quant Spectrosc Radiat Transf 2013;124:37–44.
[22] Haapanala P, Räisänen P, McFarquhar G, Tiira J, Macke A, Kahnert M, et al. Disk and circumsolar radiances in the presence of ice clouds. Atmos Chem Phys 2017;17:6865–82.
[23] Muinonen K. Scattering of light by crystals: a modified kirchhoff approximation. Appl Opt 1989;28(15):3045–50.
[24] Liu C, Panetta R, Yang P. The effects of surface roughness on the scattering properties of hexagonal columns with sizes from the Rayleigh to the geometric optics regimes. J Quant Spectrosc Radiat Transf 2013;129:169–85.
[25] Collier C, Hesse E, L T, Ulanowski Z, Penttilä A, Nousiainen T. Effects of surface roughness with two scales on light scattering by hexagonal ice crystals large compared to the wavelength: DDA results. J Quant Spectrosc Radiat Transf 2016;182:225–39.
[26] Parviainen H, Lumme K. Scattering from rough thin films: discrete-dipole-approximation simulations. J Opt Soc Am A 2007;25(1):90–7.
[27] Maradudin A. Light scattering and nanoscale surface roughness. Springer; 2007.
[28] Grynko Y, Shkuratov Y, Fönstner J. Light scattering by irregular particles much larger than the wavelength with wavelength-scale surface roughness. Opt Lett 2016;41(15):3491–4.
[29] Zhang J, Bi L, Liu J, Panetta L, Yang P, Kattawar G. Optical scattering simulation of ice particles with surface roughness modeled using the Edwards–Wilkinson equation. J Quant Spectrosc Radiat Transf 2016;178:325–35.
[30] Lindell I, Sihvola A, Muinonen K, Barber P. Scattering by a small object close to an interface. I: exact image theory formulation. J Opt Soc Am A 1991;8:472–6.
[31] Muinonen K, Sihvola A, Lindell I, Lumme K. Scattering by a small object close to an interface. II: study of backscattering. J Opt Soc Am A 1991;8:472–6.
[32] Yoneda Y. Anomalous surface reflection of X rays. Phys Rev 1963;131:2010–13.
[33] Kawanishi T, Ogura H, Wang ZL. Scattering of an electromagnetic wave from a slightly random dielectric surface: Yoneda peak and brewster angle in incoherent scattering. Waves Random Media 1997;7:351–84.
[34] Hetland S, Maradudin AA, Nordam T, Simonsen I. Numerical studies of the scattering of light from a two-dimensional randomly rough interface between two dielectric media. Phys Rev A 2016;93:053819.
[35] Kanafi M, Tuononen A. Application of three-dimensional printing to pavement texture effects on rubber friction. Road Mater Pavement 2016;18(4):865–81.
[36] Tsang L, Ding K-H, Huang S, Xu X. Electromagnetic computation in scattering of electromagnetic waves by random rough surface and dense media in microwave remote sensing of land surfaces. Proc IEEE 2013;101(2):255–79.
[37] Liang D, Xu P, Tsang L, Gui Z, Chen K. Electromagnetic scattering by rough surfaces with large heights and slopes with applications to microwave remote sensing of rough surface over layered media. Prog Electromagn Res 2013;95:199–218.
[38] Shepard M, Campbell B. Radar scattering from a self-affine fractal surface: near-nadir regime. Icarus 1999;141:156–71.
[39] Kemppinen O, Nousiainen T, Lindqvist H. The impact of surface roughness on scattering by realistically shaped wavelength-scale dust particles. J Quant Spectrosc Radiat Transf 2015;150:55–67.
[40] Nousiainen T, Muñoz O, Lindqvist H, Mauno P, Videen G. Light scattering by large saharan dust particles: comparison of modeling and experimental data for two samples. J Quant Spectrosc Radiat Transf 2011;112(3):420–33. doi:10.1016/j.jqsrt.2010.09.003.
[41] Bohren C, Huffman D. Absorption and scattering of light by small particles. Wiley; 2008.
[42] Parviainen H, Muinonen K. Rough-surface shadowing of self-affine random rough surfaces. J Quant Spectrosc Radiat Transf 2007;106:398–416.
[43] Turcotte D. Fractals and chaos in geology and geophysics. 1992.
[44] Peitgen HO, Saupe D. The science of fractal Images. Springer, 1988.
[45] Simonsen I, Vandembroucq D, Roux S. Wave scattering from self-affine surfaces. Phys Rev E 2000;61:5914–17.
[46] Yordanov O, Atanasov IS. Self-affine random surfaces. Eur Phys J B 2002;29:211–15.
[47] Persson BNJ, Albohr O, Tartaglino U, Volokitin AI, Tosatti E. On the nature of surface roughness with application to contact mechanics, sealing, rubber friction and adhesion. J Phys 2005;17:R1–R62.
[48] Jahn R, Truckenbrodt H. A simple fractal analysis method of the surface roughness. J Mater 2004;145:40–5.
[49] Kanafi M, Kuosmanen A, Pellinen T, Tuononen A. Macro- and micro-texture evolution of road pavements and correlation with friction. Int J Pavement Eng 2015;16(2):168–79.
[50] Yurkin MA, Hoekstra AH. The discrete-dipole-approximation code ADDA: capabilities and known limitations. J Quant Spectrosc Radiat Transf 2011;112:2234–47.
[51] Yurkin M, Huntemann M. Rigorous and fast discrete dipole approximation for particles near a plane interface. J Phys Chem C 2015;119:29088–94.
[52] Yurkin MA, Hoekstra AH. The discrete dipole approximation: an overview and recent developments. J Quant Spectrosc Radiat Transf 2007;106:558–89.
[53] Penttilä A, Zubko E, Lumme K, Muinonen K, Yurkin M, Draine B, et al. Comparison between discrete dipole implementations and exact techniques. J Quant Spectrosc Radiat Transf 2007;106:417–36.
[54] Yurkin MA, Hoekstra AH. User manual for the discrete dipole approximation code ADDA 1.3b42014.
[55] Warren S, Brandt R. Optical constants of ice from the ultraviolet to the microwave: a revised compilation. J Geophys Res 2008;113:D14220.
[56] Ermutlu M, Muinonen K, Lumme K, Lindell I, Sihvola A. Scattering by a small object close to an interface. III: buried object. J Opt Soc Am A 1995;12(Issue 6):1310–15.
[57] Elena Eremina E, N G, Eremin Y, Helden L, Wriedt T. Total internal reflection microscopy with a multilayered interface: a light scattering model based on a discrete sources method. J Opt A 2006;8:999–1006.
[58] Muinonen K, Nousiainen T, Lindqvist H, Muñoz O, Videen G. Light scattering by Gaussian particles with internal inclusions and roughened surfaces using ray optics. J Quant Spectrosc Radiat Transf 2009;110:1628–39.